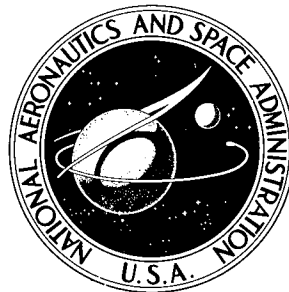


NASA TECHNICAL NOTE



NASA TN D-6610

NASA TN D-6610

CASE FILE
COPY

GENERALIZED SIMULATION TECHNIQUE
FOR TURBOJET ENGINE SYSTEM ANALYSIS

*by Kurt Seldner, James R. Mihalow,
and Ronald J. Blaha*

*Lewis Research Center
Cleveland, Ohio 44135*

1. Report No. NASA TN D-6610		2. Government Accession No.		3. Recipient's Catalog No.	
4. Title and Subtitle GENERALIZED SIMULATION TECHNIQUE FOR TURBOJET ENGINE SYSTEM ANALYSIS				5. Report Date February 1972	
				6. Performing Organization Code	
7. Author(s) Kurt Seldner, James R. Mihaloew, and Ronald J. Blaha				8. Performing Organization Report No. E-5998	
				10. Work Unit No. 132-15	
9. Performing Organization Name and Address Lewis Research Center National Aeronautics and Space Administration Cleveland, Ohio 44135				11. Contract or Grant No.	
				13. Type of Report and Period Covered Technical Note	
12. Sponsoring Agency Name and Address National Aeronautics and Space Administration Washington, D. C. 20546				14. Sponsoring Agency Code	
15. Supplementary Notes					
16. Abstract <p>A nonlinear analog simulation of a turbojet engine was developed. The purpose of the study was to establish simulation techniques applicable to propulsion system dynamics and controls research. A schematic model was derived from a physical description of a J85-13 turbojet engine. Basic conservation equations were applied to each component along with their individual performance characteristics to derive a mathematical representation. The simulation was mechanized on an analog computer. The simulation was verified in both steady-state and dynamic modes by comparing analytical results with experimental data obtained from tests performed at the Lewis Research Center with a J85-13 engine. In addition, comparison was also made with performance data obtained from the engine manufacturer. The comparisons established the validity of the simulation technique.</p>					
17. Key Words (Suggested by Author(s)) Aircraft and propulsion systems			18. Distribution Statement Unclassified - unlimited		
19. Security Classif. (of this report) Unclassified		20. Security Classif. (of this page) Unclassified		21. No. of Pages 66	
				22. Price* \$3.00	

* For sale by the National Technical Information Service, Springfield, Virginia 22151

CONTENTS

	Page
<u>SUMMARY</u>	1
<u>INTRODUCTION</u>	1
<u>ENGINE DESCRIPTION</u>	2
<u>ANALYTICAL MODEL</u>	4
GENERAL GAS DYNAMIC EQUATIONS	4
COMPRESSOR	5
Description	5
Schematic Model	5
Mathematical Model	6
Simulation Model	8
COMBUSTOR	12
Description	12
Performance	13
Pressure drop	13
Heat addition	13
Efficiency	13
Schematic Model	14
Mathematical Model	16
Simulation Model	17
TURBINE	17
Description	17
Schematic Model	17
Mathematical Model	21
AFTERBURNER	22
EXHAUST NOZZLE	23
Schematic Model	23
Mathematical Model	23
Simulation Model	24
ROTOR DYNAMICS	24
<u>SIMULATION VERIFICATION</u>	25
STEADY-STATE PERFORMANCE	25
Compressor Mapping	25
Compressor Stall	26
Engine Performance	30

DYNAMIC PERFORMANCE	30
Rotor Speed Effects	30
Combustor	31
Compressor	38
<u>SUMMARY OF RESULTS</u>	38
<u>APPENDIXES</u>	
A - SYMBOLS	40
B - BASIC GAS DYNAMICS REPRESENTATION	43
C - STEADY-STATE COMPRESSOR STAGE REPRESENTATION	45
D - STAGE GAS DYNAMICS	49
E - BIVARIANT FUNCTION GENERATION	53
F - TURBINE PERFORMANCE CORRELATION	56
REFERENCES	63

GENERALIZED SIMULATION TECHNIQUE FOR TURBOJET ENGINE SYSTEM ANALYSIS

by Kurt Seldner, James R. Mihalow, and Ronald J. Blaha
Lewis Research Center

SUMMARY

A nonlinear analog simulation of a turbojet engine was developed. The purpose of the study was to establish simulation techniques applicable to propulsion system dynamics and controls research.

A schematic model was derived from a physical description of a J85-13 turbojet engine. Basic conservation equations were applied to each component along with their individual performance characteristics to derive a mathematical representation. The simulation was mechanized on an analog computer.

The simulation was verified in both steady-state and dynamic modes by comparing analytical results with experimental data obtained from tests performed at the Lewis Research Center with a J85-13 engine. In addition, comparison was also made with performance data obtained from the engine manufacturer. The comparisons established the validity of the simulation technique.

INTRODUCTION

The requirements in supersonic aircraft for high propulsion system performance can result in normal engine operation close to compressor stall and inlet operation close to unstart. To assure satisfactory overall operation under such conditions, propulsion system design not only must include the dynamics of the inlet, engine, and associated controls but must also include the dynamic interaction between these system components. Consideration should be given to propulsion system design problems in the preliminary phases of any development program. Mathematical modeling and system simulation are generally used to resolve propulsion system design problems throughout a development program. In this way, expensive wind-tunnel and flight-test programs can be minimized, and system problems may be avoided or minimized. This

report presents the development of mathematical modeling and simulation techniques for jet engine representation in an overall propulsion system study.

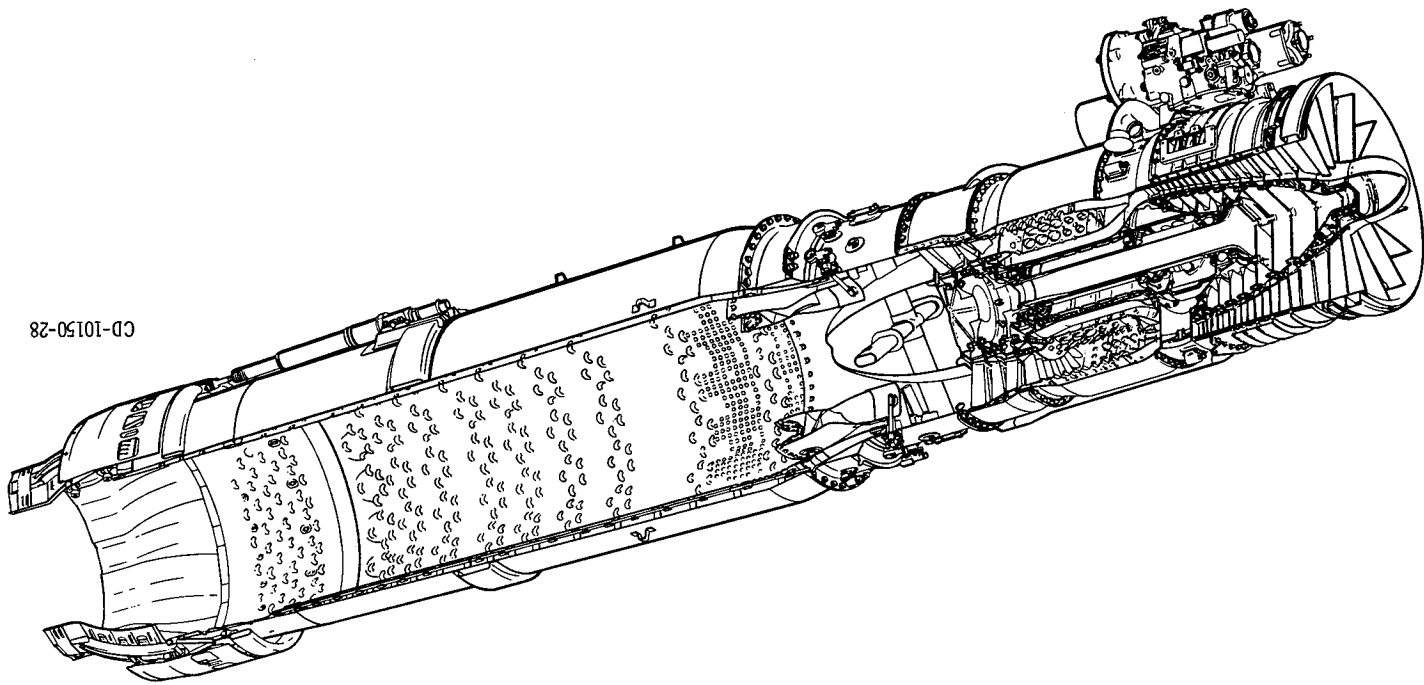
Turbojet engine simulations have been developed by both engine manufacturers and government agencies. Generally, however, the models use linear transfer function techniques for system dynamics and overall performance maps for component steady-state behavior. Such representations of system dynamics are satisfactory for engine controls development and low-frequency (10 Hz or less) system analysis. But inlet flow and shock position dynamics tend to contain significant dynamics at higher frequencies. Engine representations for use in overall propulsion system studies should thus be valid for frequencies up to 50 hertz or more. The purpose of the study was to apply recently developed (refs. 1 and 2) high-frequency compressor modeling techniques to a complete jet engine model. In this way a simulation model more suitable for overall propulsion-system analysis than the linear transfer function approach could be established.

This report proposes and develops simulation techniques applicable to any air-breathing engine. The jet engine simulation is capable of satisfying the following requirements: (1) representing the engine operating range from idle to rated speed, (2) representing engine dynamics to at least 50 hertz, and (3) representing engine operation accurately at operating conditions off the normal engine operating line. The methods developed are applied to a J85-13 engine. Results obtained from the simulation are compared with experimental data. Agreement is demonstrated between the simulation and the experimental data to frequencies as high as 60 hertz.

ENGINE DESCRIPTION

The simulation techniques developed in this report are applied to the J85-13 engine. The J85 is an afterburning, turbojet engine with an eight-stage axial-flow compressor and a two-stage turbine. Compressor discharge air that bypasses the combustion zone is used to cool combustor and turbine components. The engine, for which a cutaway section is shown in figure 1 also has variable inlet guide vanes, controlled interstage bleeds, and a variable-area exhaust nozzle. Engine control is provided through hydro-mechanical main and afterburner fuel controls and the variable-area exhaust nozzle.

The engine simulation included the compressor variable geometry features but did not include afterburner combustion. The gas dynamics for the afterburner volume, however, were included.



CD-10150-28

Figure 1. - Cutaway section of J85-13 turbojet engine and afterburner.

ANALYTICAL MODEL

For a dynamic simulation to be valid over a wide operating range, the simulation must exhibit realistic steady-state behavior over the entire operating range. Component steady-state operation can be determined from steady-state maps expressed in terms of various flow and thermodynamic parameters. The data for such maps are, in general, obtained from experimental data, although, in the early phases of a program, it may have been obtained from design studies.

In this study system flow dynamics are included with the steady-state component maps without changing the steady-state operating conditions. The dynamics are included in such a manner as to separate the component maps and help avoid algebraic loops or iterations that might otherwise be encountered. Where possible, the system dynamics are formulated in terms of the same variables used in the component maps, thus simplifying the overall simulation.

GENERAL GAS DYNAMIC EQUATIONS

The basic representations used for the system gas dynamics can be derived from conservation equations. For quasi-one-dimensional flow the basic continuity, momentum, and energy equations can be written as

$$\frac{\partial}{\partial t} (\rho_s A) + \frac{\partial}{\partial x} (\rho_s A v) = 0 \quad (1)$$

$$\frac{\partial}{\partial t} (\rho_s A v) + \frac{\partial}{\partial x} (\rho_s A v^2) = - A g \frac{\partial P_s}{\partial x} \quad (2)$$

$$\frac{\partial}{\partial t} (\rho_s A u_t) + \frac{\partial}{\partial x} (\rho_s A v h) = 0 \quad (3)$$

The symbols used in these equations and throughout the text are defined in appendix A. The conservation relations in the form of equations (1) to (3) do not include friction losses, work done on or by the fluid, or the effects of external heat. However, these effects are in general included in the component maps.

In the transition from the partial-derivative distributed-parameter form (eqs. (1) to (3)) to the total-derivative lumped-parameter form used in system simulation, the working variables must be chosen. Compressor and turbine maps are generally based

on total pressures and temperatures and on flow; thus, these variables were selected as the basic system parameters. Although some approximations (discussed later in the text) were used in the translation from static to total quantities, in general, this choice of system variables was satisfactory.

It is shown in appendix B that equations (1) to (3) can be approximated in lumped parameter form by

$$\frac{d}{dt} (\rho_s) = - \frac{1}{V} \Delta \dot{W} \quad (4)$$

$$\frac{d}{dt} (\dot{W}) = - \frac{A g}{l} \Delta P_s \quad (5)$$

$$\frac{d}{dt} (\rho_s T_t) = - \frac{\gamma}{V} \Delta (T_t \dot{W}) \quad (6)$$

Equations (4) to (6) and an equation of state form the basis for the lumped-volume gas dynamics used in the simulation.

COMPRESSOR

Description

The J85 compressor consists of eight stages with variable inlet guide vanes and interstage bleed flow. The first-stage pressure rise and flow characteristics and, in turn, the overall compressor map are thus functions of inlet guide vane angle. The overall compressor map is also a function of bleed flow. Such variable geometry features can greatly complicate compressor simulation. The stage stacking approach, however, can be used to avoid some of this complexity.

Schematic Model

Compressor modeling can be achieved by several known techniques. A proven method involves the simulation of an overall compressor map. Such maps can provide pressure, temperature, and stall information as a function of inlet parameters and engine speed. However, this technique provides only steady-state performance and, thus, does not consider interstage gas dynamics.

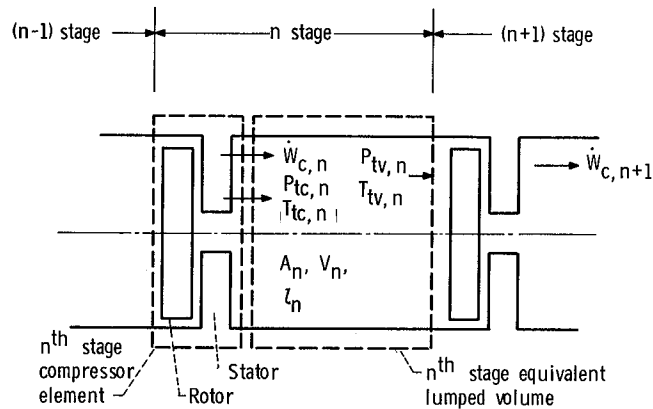


Figure 2. - Schematic of n^{th} compressor stage.

Another method of representing multistage axial-flow compressors is based on individual stage modeling and on computing the pressure and temperature rise across each stage. These stages are interconnected, or stacked, to form the compressor model where the discharge conditions of one stage are used as the inlet conditions to the following stage. The gas dynamics are readily included by considering a volume associated with each stage.

The stage stacking technique has several advantages over other simulation methods. The main advantage is that only functions of one variable must be considered. Each stage can be represented by a pair of pressure and temperature rise maps followed by its appropriate stage volume. Continuity, momentum, and energy equations are then used to compute the dynamic characteristics of each stage. A second advantage is that variable inlet geometry and interstage bleed can easily be included in the simulation. In addition, with the inclusion of the gas dynamics, the compressor simulation becomes unstable for certain operating conditions. The locus of these critical pressure ratios matches the actual compressor stall line (ref. 2). The disadvantage of this simulation technique is that a relatively large analog computer facility is required. Also, because of the large amount of nonlinear equipment, such as multipliers and function generators, the overall steady-state accuracy of the compressor model is limited.

An idealized stage is shown schematically in figure 2. In essence, the basic assumption is that each compressor stage consists of a stage and its associated volume. The mathematical analyses for the static and dynamic performance are presented in appendixes C and D.

Mathematical Model

The stage stacking technique just discussed was used for the J85 compressor simu-

lation. As mentioned previously, this method is suited for this application because it readily permits the inclusion of the gas dynamics to study compressor stability. The compressor stage characteristics are presented as nondimensionalized pressure and temperature coefficients as functions of a flow coefficient. These coefficients are defined by the relations

$$\psi_n^P = \frac{C_n T_{tv, n-1}}{N^2} \left[\left(\frac{P_{tc, n}}{P_{tv, n-1}} \right)^{2/7} - 1 \right] \quad (7)$$

$$\psi_n^T = \frac{C_n}{N^2} (T_{tc, n} - T_{tv, n-1}) \quad (8)$$

$$\varphi_{c, n} = \frac{K_n}{N} v_{zc, n} \quad (9)$$

where

$$C_n = 2gJc_p \left(\frac{\alpha}{\pi r_{T, n}} \right)^2 \quad (10)$$

$$K_n = \frac{\alpha}{\pi r_n} \quad (11)$$

The axial component of the stage inlet air flow v_z appearing in equation (9) must be determined to compute the flow function φ . This relation is derived in appendix C as

$$v_{zc, n} = \frac{\dot{W}_{c, n} R T_{sv, n-1}}{A_{c, n} P_{sv, n-1}} \quad (12)$$

The pressure and temperature for equation (12) are defined in static parameters. Because the compressor simulation is in terms of total parameters, an equivalent expression for v_z was derived in appendix C as

$$\frac{\dot{W}_{c, n} \sqrt{\theta_{v, n-1}}}{\delta_{v, n-1} A_{c, n}} = \frac{v_{zc, n}}{\sqrt{\theta_{v, n-1}}} \left[1 - \left(\frac{v_{zc, n}}{\sqrt{\theta_{v, n-1}}} \right)^2 \frac{1}{2gJc_p T_{tr} \cos^2 \beta_\eta} \right]^{1/(1-\gamma)} \rho_{tr} \quad (13)$$

The dynamic characteristics of the compressor were simulated by assuming an individual volume for each compressor stage. This volume was considered to be downstream of each stage. The dynamic characteristics were obtained by applying continuity, momentum, and energy equations. The relations used for the gas dynamics were derived in appendix D as

$$\frac{d}{dt} (\rho_{sv,n}) = \frac{1}{V_n} (\dot{W}_{c,n} - \dot{W}_{c,n+1} - \dot{W}_{b,n}) \quad (14)$$

$$\frac{d}{dt} (\dot{W}_{c,n}) = \frac{A_n g}{l_n} (P_{tc,n} - P_{tv,n}) \quad (15)$$

$$\frac{d}{dt} (\rho_{sv,n} T_{tv,n}) = \frac{\gamma}{V_n} (T_{tc,n} \dot{W}_{c,n} - T_{tv,n} \dot{W}_{c,n+1} - T_{tv,n} \dot{W}_{b,n}) \quad (16)$$

The equation of state for the n^{th} volume is as follows:

$$P_{tv,n} = R \rho_{sv,n} T_{tv,n} \quad (17)$$

The interstage bleed was computed for the third, fourth, and fifth stages by assuming that the bleed ports were choked. The bleed flow can be computed from the relation

$$\dot{W}_{b,n} = k_b A_{b,n} \frac{P_{tv,n}}{\sqrt{T_{tv,n}}} \quad (18)$$

Simulation Model

The eight stages of the J85 compressor were simulated by using equations (7) to (11) and (13) to (18) combined with the appropriate pressure and temperature maps. The compressor stage maps are presented in terms of a pressure coefficient ψ^P and a temperature coefficient ψ^T as functions of a flow coefficient ϕ . Typical curves for the second stage of the J85 compressor are presented in figure 3. These curves must be entered through the flow function so that a single-valued output results. The flow function ϕ can be computed from equations (9) and (13).

The air angle β , which appears in equation (13), varies as a function of corrected speed. The angles were assumed to be constant over the normal operating range of the

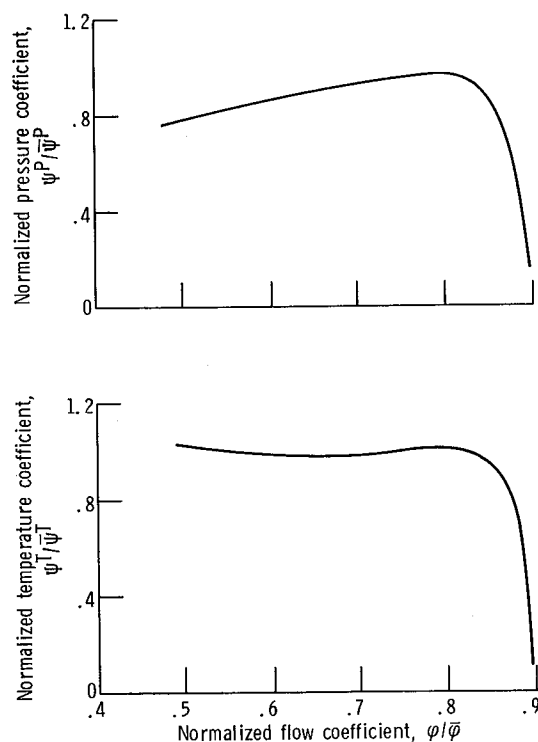


Figure 3. - Pressure and temperature maps for second stage of compressor.

J85 engine because the deviations from average values were small.

Equation (13) was solved on a digital computer for v_z as a function of inlet air flow and angle β . The results were approximated with a quadratic expression having a standard error of estimate of 2.93 meters per second (9.62 ft/sec). A typical curve for the analog simulation is presented in figure 4.

The stage maps for the first compressor stage must be modified to account for the effects of inlet guide vane variations. First-stage pressure and temperature characteristics were generated for closed, half open, and full open inlet guide vane positions, for which the pressure maps are shown in figure 5. The pressure and temperature characteristics were then determined by interpolating between these curves. A detailed discussion of this and several other techniques for bivariant function generation is presented in appendix E.

Interstage bleed was included in the third, fourth, and fifth compressor stages. The choked flow equation (18) was used to compute the actual bleed flow. The area of the bleed ports was scheduled as a function of corrected speed and compressor inlet temperature. The bleed valve movement occurs within the 80 to 100 percent of the corrected speed range.

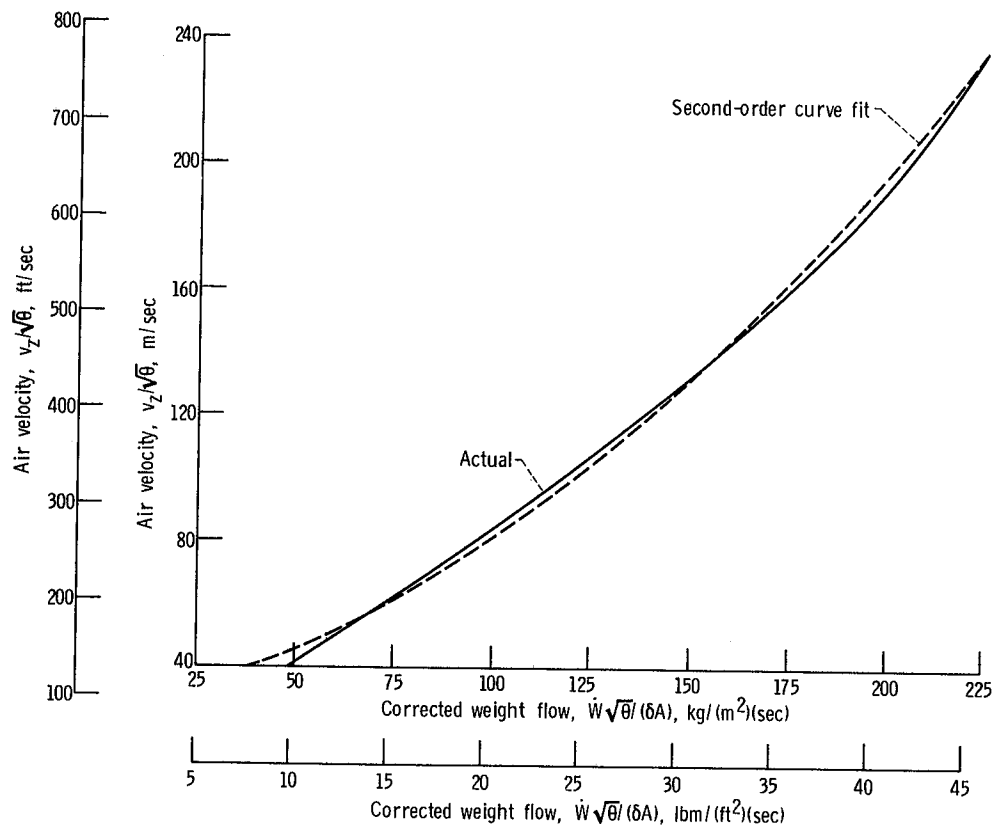


Figure 4. - Typical air velocity computation.

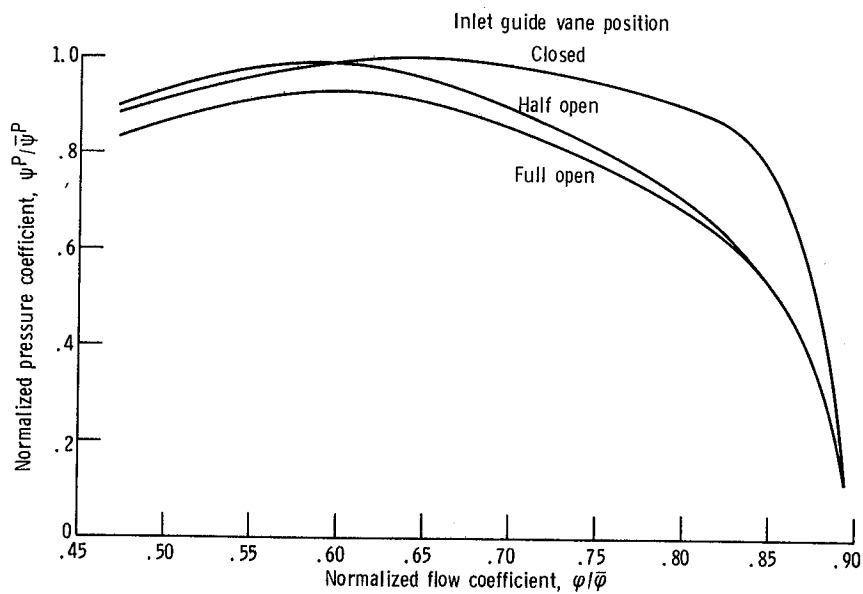


Figure 5. - First stage pressure map for various inlet guide vane positions.

The outlet guide vanes were represented by a volume and pressure drop. The temperature within the guide vane volume was assumed to be that of the compressor discharge.

A block diagram of a typical compressor stage showing the computational techniques used in the simulation is presented in figure 6. As observed, the stage inlet conditions are used to compute the value of the flow function. This value was then used to determine the stage pressure and temperature coefficients from which the discharge condi-

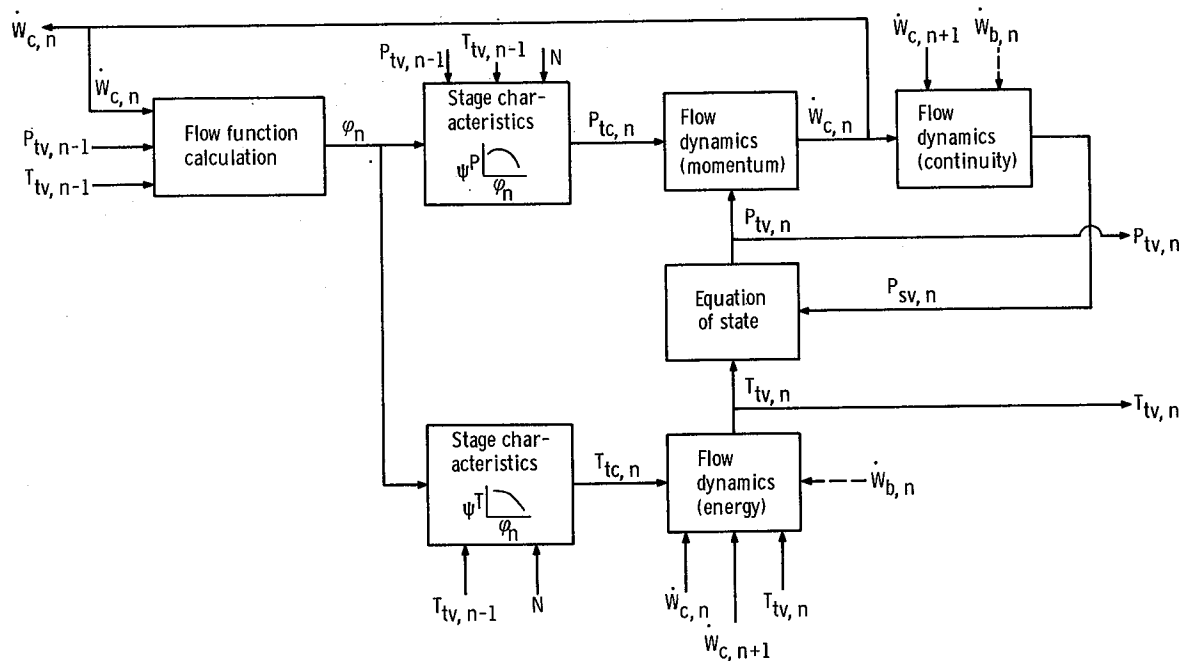


Figure 6. - Block diagram for simulation of n^{th} compressor stage dynamics.

tions were computed. The stage discharge conditions combined with the gas dynamics are used to compute the pressures and temperatures of each stage volume. These parameters were then used for the inlet conditions to the next stage.

The pressures and temperatures in the compressor simulations are computed in terms of total parameters. The simulation neglects the difference between static and total parameters because of the complexity involved in computing the Mach number for each stage. Further discussion is presented in appendix D and reference 2.

COMBUSTOR

Description

The J85 annular combustor is shown in figure 7. Air from the compressor enters the liner through perforations (thimble holes) and louvers. The thimble holes direct air into the burning area (primary combustion flow), while the louvers provide a boundary layer (secondary cooling flow) of comparatively cool air along the inner surface of the liner.

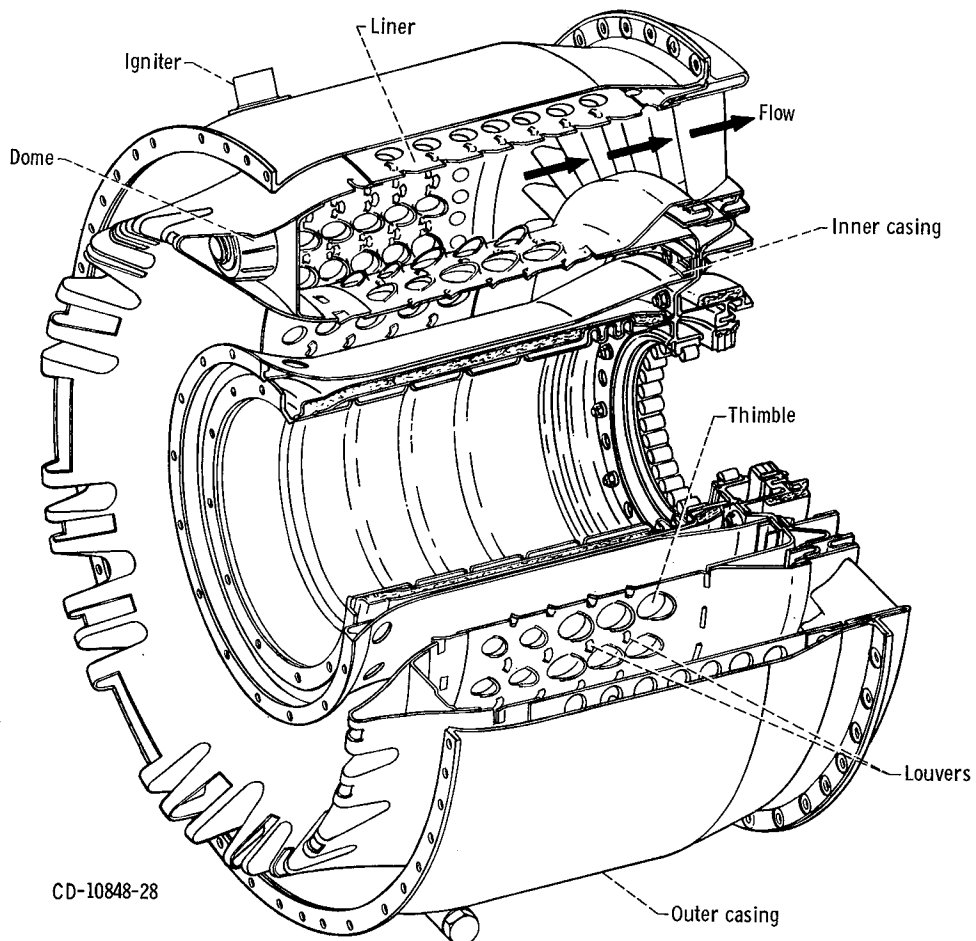


Figure 7. - J85-13 combustor.

Performance

In modeling the combustor steady-state operation pressure drop, heat addition and combustor efficiency must be accounted for.

Pressure drop. - The total pressure drop across a combustor can be attributed to fluid friction and momentum loss due to heat addition and stream mixing. The analytical representation is based on the assumption that the combustion chamber can be divided into equivalent fluid friction and heat addition zones. The air enters the combustion zone and experiences a total pressure drop due to friction. This pressure drop corresponds to the actual mixing drop that occurs without combustion, which can be determined experimentally and correlated with theory. Momentum pressure loss is assumed to occur in the combustion zones with the addition of heat to the air. This drop is assumed to occur after the friction loss. The overall loss in pressure is then formed from the sum of the two losses. The resulting expression is

$$\Delta P_{t,4} = \frac{\dot{W}_3^2}{P_{t,3}} (K_A T_{t,3} + K_B T_{t,4}) \quad (19)$$

where K_A and K_B are experimentally determined coefficients peculiar to each combustor: K_A is found from noncombustion flow tests, and K_B from combustion flow tests.

Heat addition. - The actual combustion involves processes such as atomization, vaporization, mixing, and chemical reaction. These processes are gradual in time and space. For combustor simulation, however, it is only necessary to determine relations between initial and final conditions.

Since variations in specific heat due to composition and temperature changes can introduce significant errors, variable specific heat is considered in the combustor performance. However, it is assumed that

$$h_4 = f(T_{t,4}) \quad (20)$$

Using data obtained from reference 3, this functional relation was evaluated and is plotted in figure 8.

Efficiency. - Because of the complexity of the combustion process, no exact analytical treatment of combustor efficiency was attempted. For the purposes of this simulation, combustor efficiency was approximated by a correlation of the form

$$\eta_4 = f(P_{t,4} \Delta T_{t,4}) \quad (21)$$

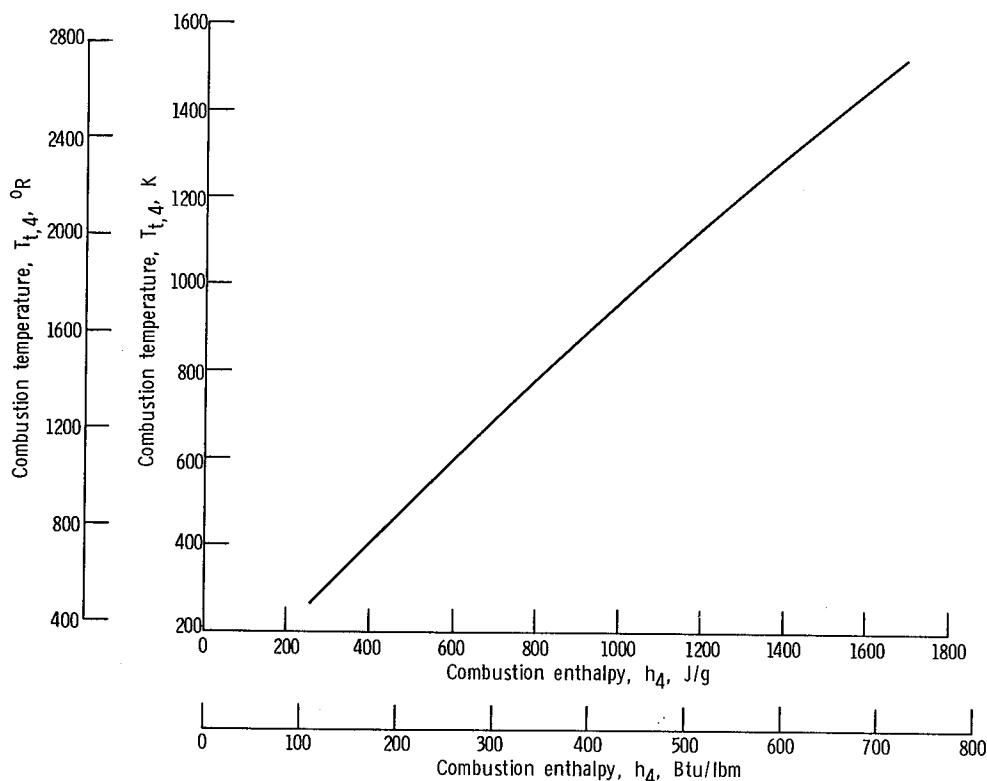


Figure 8. - Temperature of combustion gas as function of enthalpy.

The efficiency η_4 is here defined as that portion of the heat of combustion that is available for a gas temperature rise. The parameter $P_{t,4} \Delta T_{t,4}$ is based on ideal combustion temperature rise and includes the effects of fuel-to-air ratio and inlet pressure variations but neglects the effect of inlet temperature variation.

Combustor efficiency for the J85 is shown in figure 9. Steady-state data on and near the operating line at sea level and altitude were used to generate the relation. It provides reasonable accuracy over a wide range of operating conditions.

Schematic Model

The combustor model used in this simulation is formed by adding dynamics to the steady-state characteristics presented in the performance section. The combustor is lumped into a single equivalent one-dimensional volume. The volume is bounded by the inner and outer shells, with its length being defined by the compressor exit face and the turbine first-stage stator face.

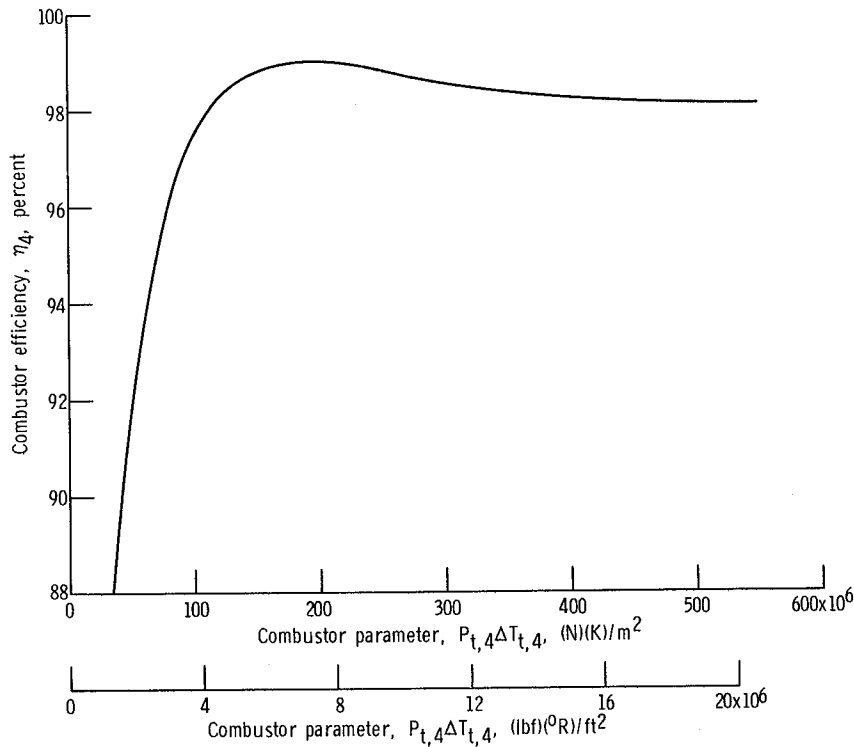


Figure 9. - Combustor efficiency representation.

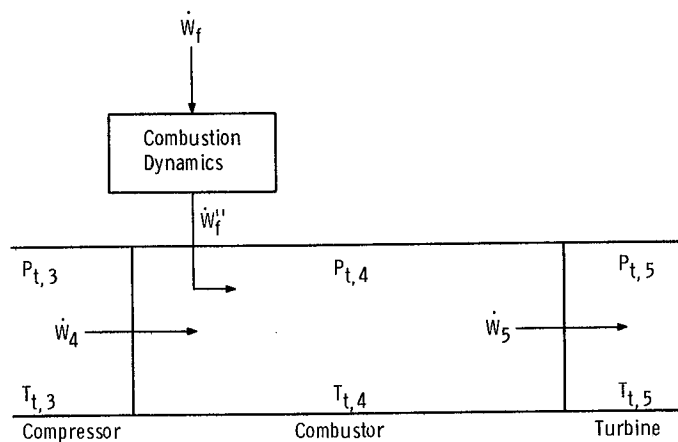


Figure 10. - Combustor model.

In the formation of the combustor model through the addition of dynamics to the steady-state characteristics, provision is made for heat addition. The combustion process is assumed to be continuous in time and external to the basic combustor gas dynamic lumped volume. The end product of the combustion process is assumed to be heat, which is added to the lumped volume. Schematically, this representation is shown in figure 10.

Mathematical Model

Applying the basic equations of momentum and energy to the schematic model results in the following mathematical representation: for combustor weight flow the momentum equation yields

$$\frac{d\dot{W}_4}{dt} = \frac{gA_4}{l_4} \left[(P_{t,3} - P_{t,4}) - \Delta P_{t,4} \right] \quad (22)$$

where

$$\Delta P_{t,4} = \frac{K_C \dot{W}_4^2}{P_{t,3}} (0.771 T_{t,3} - 0.085 T_{t,4}) \quad (23)$$

The constants in this equation are empirically determined from J85 turbojet experimental data.

The energy equation gives

$$\frac{d}{dt} (\rho_{s,4} T_{t,4}) = \frac{\gamma}{V_4} \left(\dot{W}_4 T_{t,3} + \dot{W}_f'' T_{t,4} - \dot{W}_5 T_{t,4} + \frac{\eta_4}{c_p} \dot{W}_f'' h_c \right) \quad (24)$$

Combustion limits were not included in this representation.

The fuel flow \dot{W}_f'' is the result of combustion dynamics imposed on the fuel flow external to the lumped volume gas dynamics.

$$\frac{\dot{W}_f''}{\dot{W}_f} = \frac{K e^{-\sigma s}}{(1 + \tau_A s)(1 + \tau_B s)} \quad (25)$$

where τ_A and τ_B are the time constants associated with heat release due to combustion lag. The delay time σ is associated with the ignition lag and transport delay due to the difference between where the fuel flow is measured and where the fuel nozzle is.

The continuity equation gives

$$\frac{d}{dt} (\rho_{s,4}) = \frac{1}{V_4} (\dot{W}_4 + \dot{W}_f'' - \dot{W}_5) \quad (26)$$

Simulation Model

The mathematical representation was simulated on the analog computer in a straight forward manner.

The burner efficiency curve shown in figure 9 was approximated using a diode function generator. The fuel flow dead time was generated using a fourth-order Padé approximation.

TURBINE

Description

The J85-13 engine uses a two-stage turbine cooled by secondary combustion air. The most direct approach to turbine modeling would have been to apply a stage stacking technique, similar to that used for the compressor, to the two turbine stages. Individual stage data for the turbine were not available, however, and it was thus necessary to represent the turbine from overall performance data.

Schematic Model

The turbine data available during the J85 simulation program was in the form of an overall performance map. These data are plotted in figure 11. The direct application of information in this form would be extremely difficult on an analog computer. To avoid this problem the data were manipulated to a form more amenable to analog simulation techniques.

The data in the performance map of figure 11 can be regarded as giving a turbine enthalpy parameter and turbine efficiency as functions of flow and speed parameters; that is,

$$\frac{\Delta h_5}{T_{t,4}} = f_{(1)} \left(\frac{\dot{W}_4 \sqrt{T_{t,4}}}{P_{t,4}}, \frac{N}{\sqrt{T_{t,4}}} \right) \quad (27)$$

$$\eta_5 = f_{(2)} \left(\frac{\dot{W}_4 \sqrt{T_{t,4}}}{P_{t,4}}, \frac{N}{\sqrt{T_{t,4}}} \right) \quad (28)$$

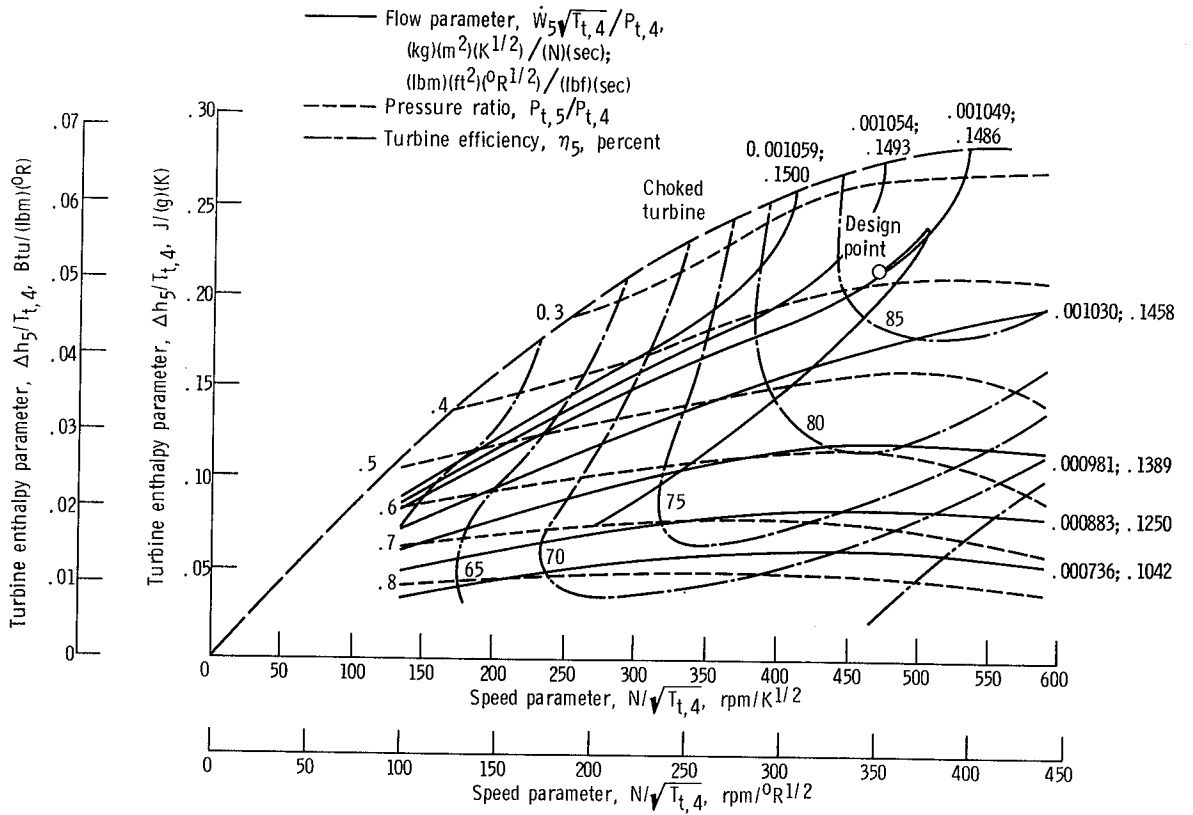


Figure 11. - Overall turbine performance map.

The turbine efficiency η_5 can be defined as

$$\eta_5 = \frac{\Delta h_5}{\Delta h'_5} \quad (29)$$

where $\Delta h'_5$ is the ideal isentropic enthalpy drop. Using the isentropic relation between pressure and temperature, the pressure ratio across the turbine can be expressed as

$$\frac{P_{t,5}}{P_{t,4}} = \left(1 - \frac{\Delta h_5}{\eta_5 c_p T_{t,4}} \right)^{\gamma/(\gamma-1)} \quad (30)$$

Considering equations (27) to (30), it can be concluded that

$$\frac{\Delta h_5}{T_{t,4}} = f(1) \left(\frac{P_{t,5}}{P_{t,4}}, \frac{N}{\sqrt{T_{t,4}}} \right) \quad (31)$$

$$\frac{\dot{W}_5 \sqrt{T_{t,4}}}{P_{t,4}} = f_{(2)} \left(\frac{P_{t,5}}{P_{t,4}}, \frac{N}{\sqrt{T_{t,4}}} \right) \quad (32)$$

These functions are shown in figures 11 and 12. The enthalpy parameter is superimposed on the overall performance map.

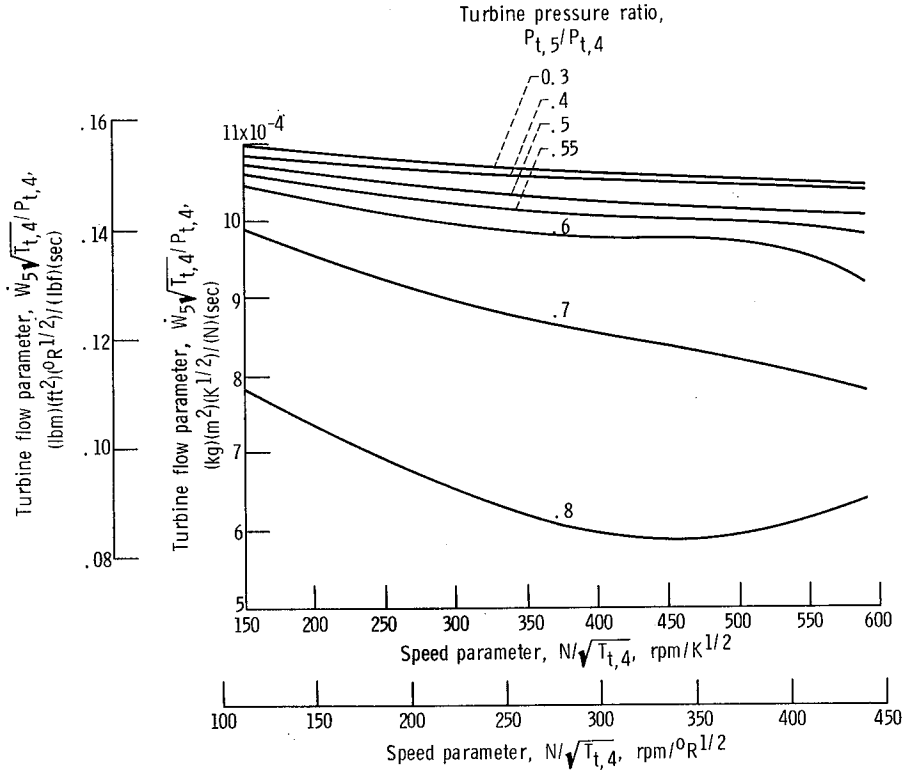


Figure 12. - Turbine flow performance.

The functional relations of equations (31) and (32) were normalized with a turbine speed parameter to separate and make them well behaved for the simulation. The resulting curves are plotted in figures 13 and 14. In this representation, the enthalpy function becomes a torque parameter, that is,

$$\frac{\Delta h_5}{N \sqrt{T_{t,4}}} \propto \frac{L_5}{\dot{W}_4 \sqrt{T_{t,4}}} = f_{(3)} \left(\frac{P_{t,5}}{P_{t,4}}, \frac{N}{\sqrt{T_{t,4}}} \right) \quad (33)$$

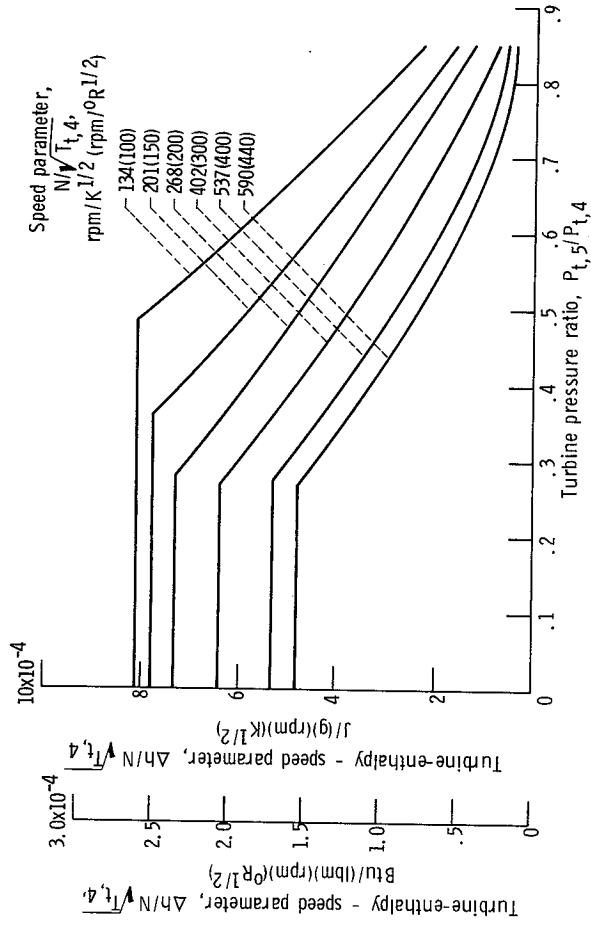


Figure 13. - Turbine torque characteristics.

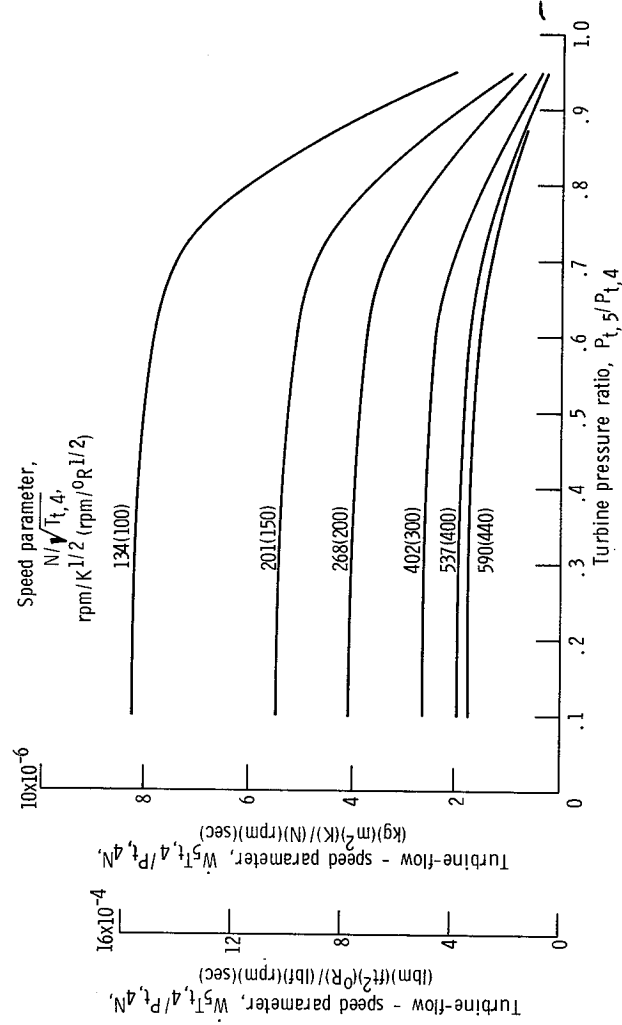


Figure 14. - Turbine normalized flow characteristics.

and the normalized flow parameter becomes

$$\frac{\dot{W}_5 T_{t,4}}{NP_{t,4}} \propto \frac{\dot{W}_5}{N\rho_{s,4}} = f_{(4)}\left(\frac{P_{t,5}}{P_{t,4}}, \frac{N}{\sqrt{T_{t,4}}}\right) \quad (34)$$

An attempt at a correlation leading to a function of a single variable is presented in appendix F. The results of this correlation were good, but not accurate enough for this case to duplicate known steady-state data. Therefore, the two-variable correlation was used.

No attempt is made to model the actual turbine cooling flow process. The flow is instead added to the appropriate volume and mixed. The momentum of the stream is neglected. Since performance is based on inlet flow, no appreciable error is introduced. The turbine model is shown schematically in figure 15.

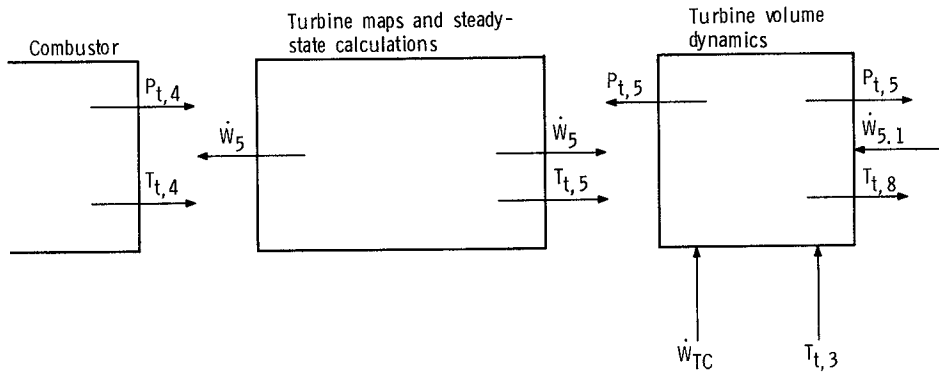


Figure 15. - Turbine model.

Mathematical Model

The turbine is represented mathematically by the imposition of the basic conservation equations on the turbine steady-state performance characteristics. Input variables and concurrent output values are used to calculate steady-state values of the enthalpy and flow parameters. The inertance is extremely low for this model, thus, the turbine flow was determined directly from the steady-state performance map

$$\frac{\dot{W}_5 T_{t,4}}{NP_{t,4}} = f_{(5)}\left(\frac{P_{t,5}}{P_{t,4}}, \frac{N}{\sqrt{T_{t,4}}}\right) \quad (35)$$

given in figure 14.

The turbine enthalpy drop is computed from

$$\frac{\Delta h_5}{N\sqrt{T_{t,4}}} = f_{(6)}\left(\frac{P_{t,5}}{P_{t,4}}, \frac{N}{\sqrt{T_{t,4}}}\right) \quad (36)$$

which is plotted in figure 13. The enthalpy drop determined in equation (36) is used to compute the turbine discharge temperature from

$$T_{t,5} = T_{t,4} - \frac{\Delta h_5}{c_p} \quad (37)$$

The pressure and temperature downstream of the turbine are determined from conservation equations written for the volume. The continuity equation yields

$$\frac{d}{dt}(\rho_{s,8}) = \frac{1}{V_8}(\dot{W}_5 + \dot{W}_{TC} - \dot{W}_8) \quad (38)$$

The energy equation is

$$\frac{d}{dt}(\rho_{s,8}T_{t,8}) = \frac{\gamma}{V_8}(T_{t,5}\dot{W}_5 + T_{t,3}\dot{W}_{TC} - T_{t,8}\dot{W}_8) \quad (39)$$

AFTERBURNER

The afterburner volume was included in the simulation; however, afterburner combustion was not considered. The lumped volume representation consisted of mass and

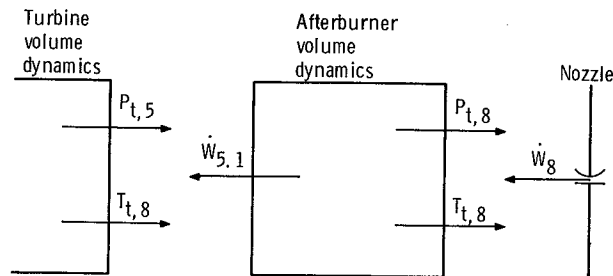


Figure 16. - Lumped volume dynamics.

momentum balances, but no energy balance. The lumped volume dynamics are shown in figure 16.

The momentum and continuity equations are

$$\frac{d}{dt} (\dot{W}_{5.1}) = \frac{A_{5.1} g}{l_{5.1}} (P_{t,5} - P_{t,8}) \quad (40)$$

$$\frac{d}{dt} (P_{t,8}) = \frac{R}{V_8} (\dot{W}_{5.1} T_{t,8} - \dot{W}_8 T_{t,8}) \quad (41)$$

Inherent in this representation is the assumption that the afterburner volume is at the same temperature as the turbine discharge.

EXHAUST NOZZLE

Schematic Model

The nozzle was simply considered as a variable-area flow passage capable of choking. It does not, as such, have an associated volume and becomes essentially the terminal boundary of the turbojet.

Mathematical Model

The nozzle is represented mathematically by the relation

$$\frac{\dot{W}_8 \sqrt{T_{t,8}}}{P_{t,8}} = K_8 f \left(\frac{P_{s,0}}{P_{t,8}} \right) \quad (42)$$

where $P_{s,0}$ is ambient static pressure. The parameter K_8 is variable and lumps the nozzle flow coefficient and nozzle area with other fluid constants. Thus, it is proportional to the nozzle area and represents the turbojet engine terminal impedance.

The function $f(P_{s,0}/P_{t,8})$ is the well-known compressible flow function:

$$f \left(\frac{P_{s,0}}{P_{t,8}} \right) = \left(\frac{P_{s,0}}{P_{t,8}} \right)^{1/\gamma} \sqrt{1 - \left(\frac{P_{s,0}}{P_{t,8}} \right)^{(\gamma-1)/\gamma}} \quad (43)$$

For pressure ratio values below critical, it becomes constant and simulates a choked passage.

Simulation Model

The compressible flow function was approximated by a fixed diode function generator. The parameter K_8 was scheduled as a function of engine speed to match the steady-state operating line.

ROTOR DYNAMICS

The operating line of a turbojet engine is the locus of steady-state performance match points between the compressor and turbine. A mismatch between these components produces an unbalanced torque or acceleration potential, which must be integrated through a dynamic relation to change the speed and seek a steady-state match.

The relation governing rotor dynamics is the conservation of angular momentum:

$$\frac{dI\omega}{dt} = \sum L \quad (44)$$

Using the expression

$$\mathcal{P} = \omega L = J \dot{\omega} \Delta h \quad (45)$$

the dynamic relation between engine speed and enthalpy change is

$$\frac{dN}{dt} = \left(\frac{30}{\pi}\right)^2 \frac{J}{NI} \sum \dot{W} \Delta h \quad (46)$$

The net sum of enthalpy differences are those that occur across the compressor and turbine, thus

$$\frac{dN}{dt} = \left(\frac{30}{\pi}\right)^2 \frac{J}{NI} \left[(\dot{W}_5 h_4 - \dot{W}_8 h_5) - (\dot{W}_3 h_3 + \dot{W}_b h_b - \dot{W}_2 h_2) \right] \quad (47)$$

where h_b is compressor bleed total enthalpy.

SIMULATION VERIFICATION

To establish the validity of the engine simulation described in this report, data obtained from three sources were compared with results obtained from the simulation. First, steady-state compressor operation and the engine system normal operating line were compared with data obtained from the manufacturer's digital engine program. Second, compressor steady-state and stall line data obtained from reference 4 were used to check the compressor model. Finally, unpublished engine system frequency response data were used to verify the engine system simulation's dynamic response.

Data for compressor operation along constant speed lines and the compressor stall line were obtained from a test program run at Lewis. The test results were obtained for an off-schedule inlet guide vane and inlet bleed configuration. Details of this test program can be found in reference 4.

Engine system frequency response data were obtained from a test program conducted in the 10- by 10-foot Supersonic Wind Tunnel. The program used a J85-13 engine and a mixed-compression supersonic inlet. Details of the inlet dynamics are presented in reference 5. The engine system was instrumented to obtain total and static pressures at various engine and inlet stations. Frequency response data were obtained by varying combustor fuel flow and recording system pressures. The frequency range of available data is limited to about 60 hertz.

STEADY-STATE PERFORMANCE

Compressor Mapping

To separate the compressor from the combustor and turbine for independent analysis, the compressor model was terminated with an equivalent volume and a choked orifice. This simplification was used during the mapping of the steady-state performance characteristics of the compressor.

The compressor performance map can be generated by varying the terminating impedance at various rotational speeds. With increasing compressor terminating impedance, caused by reductions in the choked station area, the compressor operating point moves along the constant speed line. Several constant speed lines were mapped. A representative compressor map, for a limited speed range, obtained from the simulation is presented in figure 17. As a comparison, sea-level experimental data obtained from reference 4 are also presented in this figure. Both the simulation and test results were

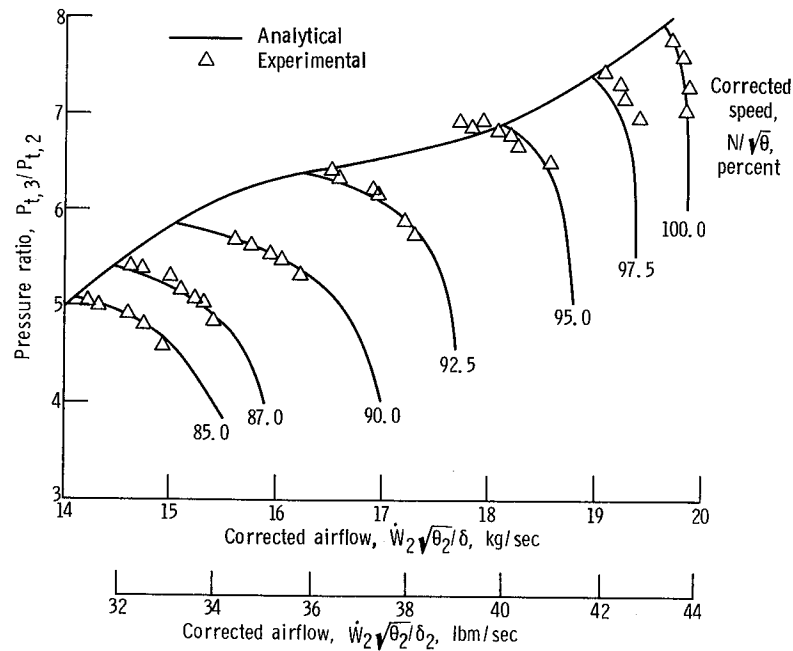


Figure 17. - Compressor map for off-schedule inlet guide vanes and interstage bleeds.

obtained for an off-schedule inlet guide vane and interstage bleed configuration. The agreement between the experimental and analytical results is good and verifies the steady-state representation of the compressor.

Compressor Stall

As described in reference 2, it was found that, as the terminating impedance was increased, the simulation will exhibit a nonlinear oscillation at an operating point on the constant speed line. Further increase in the terminating impedance causes a higher amplitude oscillation. The simulation exhibited hysteresis in that the impedance must be reduced to a level below the point of initial instability to reestablish system stability.

The locus of the operating points just before sustained oscillations is defined as the compressor stall line and is shown in figure 18. Again as a comparison, the experimental stall line is also presented. The figure indicates that the analytical and experimental stall lines compare favorably.

Some understanding of compressor performance in the vicinity of stall can be obtained from the individual stage pressure maps. The J85 normalized stage characteristics for corrected speeds of 100 and 80 percent are illustrated in figures 19 and 20, respectively. Only the first-stage characteristics are varied with the inlet guide vane position.

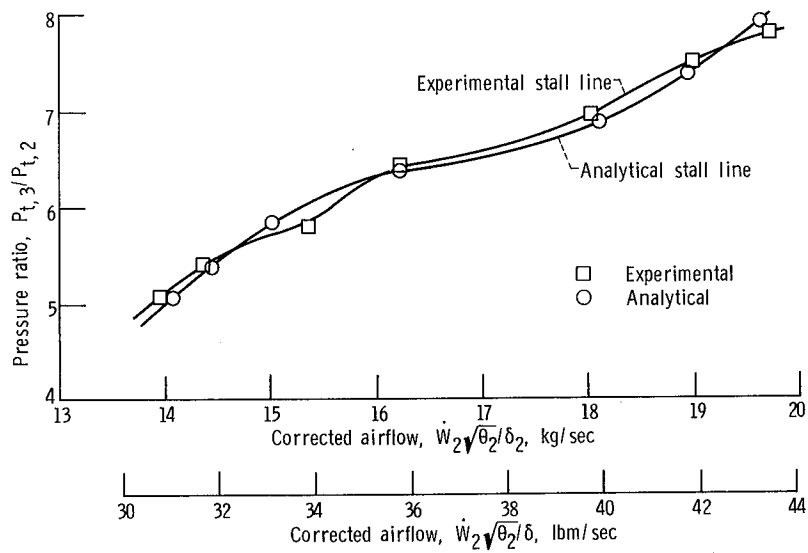


Figure 18. - Compressor stall characteristics for off-schedule inlet guide vanes and interstage bleeds.

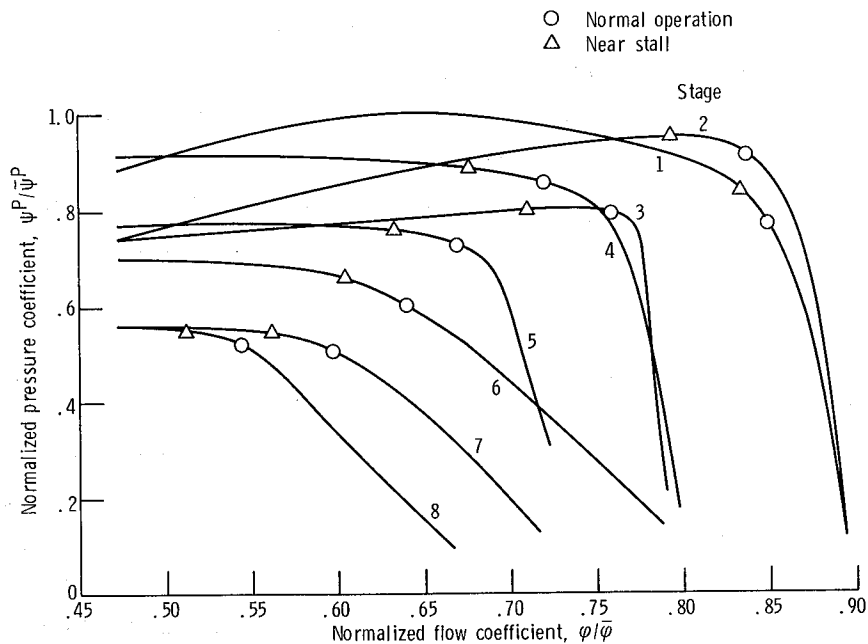


Figure 19. - Stage pressure maps including operating points for design speed.

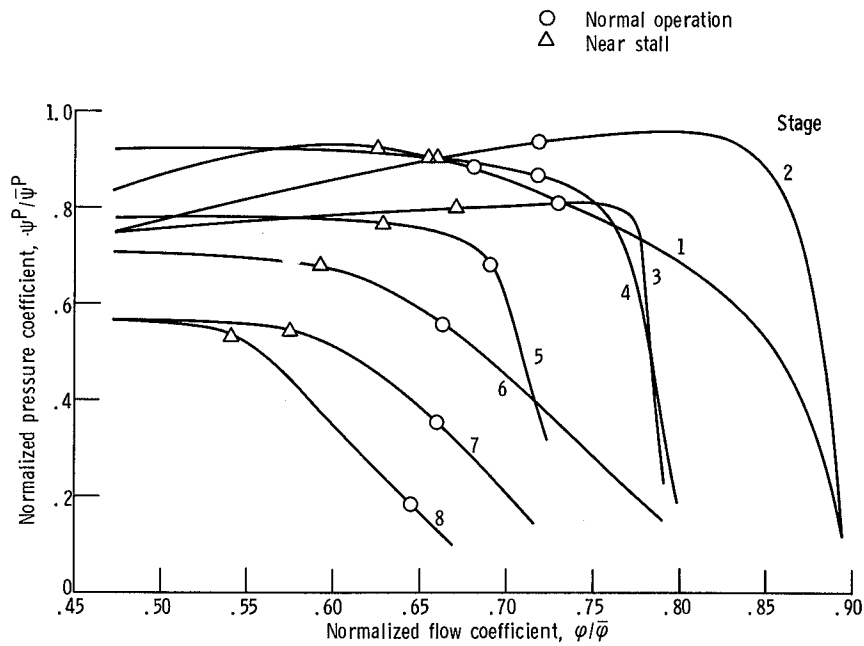


Figure 20. - Stage pressure maps including operating points for 80 percent of design speed.

The normal operating points of the various stages (equilibrium point) are indicated on the compressor stage maps. The effects of the variable geometry is evident in that the weight flow through the latter stages of the compressor is reduced at the lower engine speed. Interstage bleed increases the weight flow through the front compressor stages so as to avoid stall. With higher weight flow, the flow coefficient ϕ increases to shift the operating point to the stable region. As is also observed from these curves, at higher operating speeds most of the compressor pressure rise is achieved in the latter stages. At lower operating speeds, the pressure rise is obtained in the front stages.

As can be further observed, normal operation at the design speed occurs on the negative slope portion of the pressure-rise maps for all stages. As the stability boundary is approached, all the stages move towards a less negative slope. The second and third stages move into the positive slope region. For operation at 80 percent of design speed, normal operation of stages 2 and 3 occurs within the positive slope region. As the stability boundary is approached, these two stages shift towards increasing positive slope.

After the stability boundary is crossed, the simulation is invalid because the stage characteristics are inaccurate for stalled operation. Any degradation of the stage performance in the stalled region is not considered in this engine simulation. A detailed discussion of compressor stall can be found in reference 6.

TABLE I. - STEADY-STATE PERFORMANCE

Design engine corrected speed, percent	Type of data	Compressor discharge						Combustor						Turbine					
		Pressure		Temperature		Air flow		Pressure		Temperature		Air flow		Pressure		Temperature		Air flow	
		kN/m ²	lbf/ft ²	K	°R	kg/sec	lbm/sec	kN/m ²	lbf/ft ²	K	°R	kg/sec	lbm/sec	kN/m ²	lbf/ft ²	K	°R	kg/sec	lbm/sec
48	Experimental	161.4	3 370	338	609	6.21	13.7	153.1	3 197	837	1507	4.72	10.4	104.8	2189	765	1377	4.81	10.6
	Analytical	164.8	3 442	341	614	6.08	13.4	153.1	3 197	853	1535	4.72	10.4	105.5	2203	781	1405	4.81	10.6
80	Experimental	338.5	7 070	424	763	13.9	30.6	309.6	6 466	797	1435	11.4	25.1	126.2	2635	647	1164	11.5	25.3
	Analytical	335.8	7 013	426	767	14.5	31.9	310.9	6 494	803	1446	11.4	25.1	133.8	2794	643	1158	11.5	25.3
100	Experimental	703.8	14 700	544	979	19.9	43.9	653.1	13 640	1226	2206	19.2	42.4	246.2	5141	992	1785	19.6	43.2
	Analytical	709.6	14 820	550	990	20.0	44.0	653.1	13 640	1240	2232	19.2	42.4	264.1	5515	1021	1838	19.6	43.2

Engine Performance

To verify the complete engine simulation over its entire operating range, analytical values of pressure, temperature, and weight flow obtained from the simulation were compared with experimental values. They were also compared with steady-state data obtained from the manufacturer's overall digital performance program. The results are shown in table I.

DYNAMIC PERFORMANCE

This section presents a comparison of frequency response obtained from the engine simulation with experimental data obtained during actual engine tests in the Lewis 10-by 10-Foot Supersonic Wind Tunnel. During the tunnel test program an axisymmetric mixed-compression inlet was used with the engine. For comparison with the tunnel test data, a linear inlet representation based on the techniques of reference 7 was added to the engine model. The inlet representation is only valid for small perturbations so that the inlet was modeled for the designated engine operating conditions. The inlet was required to assure correct compressor face conditions.

In the actual test program, a long feed line was used between the high-response fuel-control valve and the engine fuel spray nozzle. Since this line introduced unwanted dynamics to the system, it was necessary to modify the experimental data and eliminate these dynamics. The frequency response curves presented in this section are therefore all referenced to the combustor fuel spray nozzle pressure.

Rotor Speed Effects

The computer representation of the J85 engine was developed to establish the capability of modeling engine system responses in the frequency range from 10 to 50 hertz. Engine system low-frequency performance is dominated by the rotor-speed - time constant. Since this time constant has a break frequency below 1 hertz, it was assumed that unpublished test data could be matched in the frequency range of interest (above 10 Hz) by operating the engine simulation at constant speed. The frequency response data presented in this report for the engine simulation were thus obtained by operating the computer model in a constant-speed mode.

To establish the validity of the assumption that rotor dynamics could be neglected in the frequency range above 10 hertz, a brief linear analysis was performed. The re-

sponse of combustor total pressures to fuel flow disturbances both with and without rotor speed effects was determined and compared. Conceptually, the response of combustor total pressure to fuel flow disturbances can be approximated by

$$\Delta P_{t,4} \approx \Delta \dot{W}_f'' \left(\frac{\partial P_{t,4}}{\partial \dot{W}_f''} + \frac{\Delta N}{\Delta \dot{W}_f''} \frac{\partial P_{t,4}}{\partial N} \right) \quad (48)$$

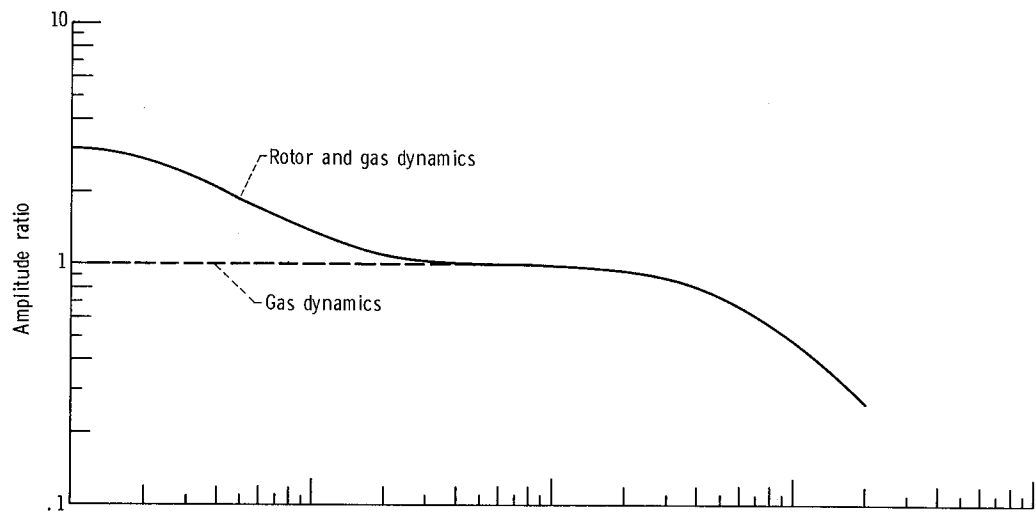
The first term of equation (48) represents the rise in combustor total pressure, which is caused by energy addition from combustion. This rise would include combustion dynamics and is characteristically fast in response. The second term represents the increase in pressure due to engine rotor dynamics, which is dominated by the rotor time constant and is thus slow in response. An approximate transfer function for this overall process can be given as

$$\frac{P_{t,4,G} + P_{t,4,N}}{\dot{W}_f''} = \frac{P_{t,4}}{\dot{W}_f''} = (K_G + K_R) \frac{\left[1 + \frac{(K_G \tau_R + K_R \tau_G)s}{K_G + K_R} \right]}{(1 + \tau_R s)(1 + \tau_G s)} \quad (49)$$

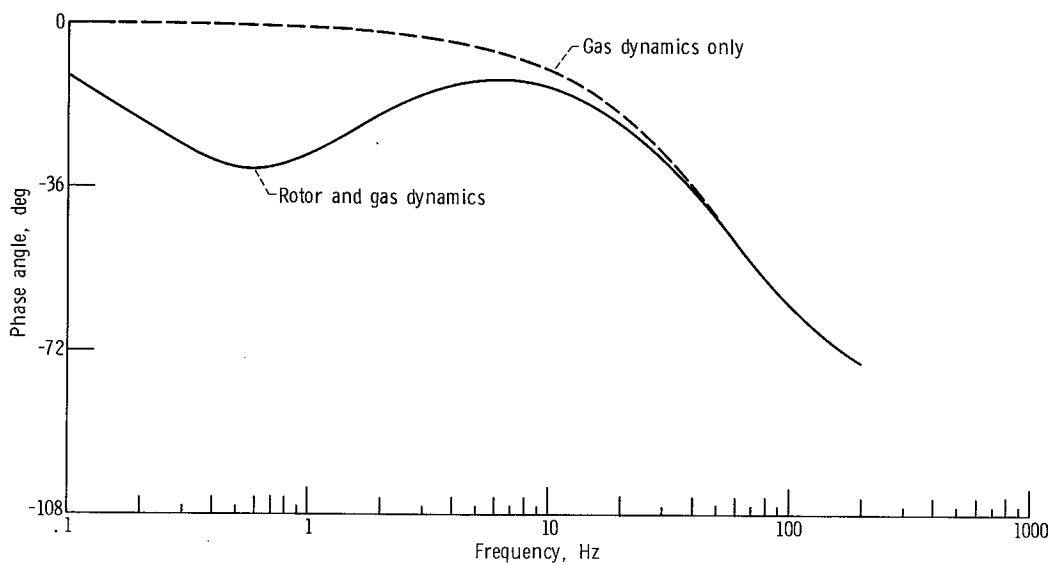
where τ_R and τ_G are the rotor and gas time constants, respectively. The combustor total-pressure frequency response, neglecting transport delays, can be determined from equation (49). The results of such a calculation using $\tau_R = 0.5$ second, $\tau_G = 2.9$ milliseconds, and appropriate gains are shown in figure 21. Also plotted in figure 21 are the results obtained from equation (48) where the rotor dynamics are neglected. As can be seen, the effects of rotor dynamics on combustor total pressure response are significant only below 5 hertz. It should be noted, however, that in the range from 5 to about 15 hertz some phase lag (7° to 2°) is added by the rotor dynamics. The use of constant rotor speed in the simulation is thus a reasonable assumption in the determination of system responses above 10 hertz.

Combustor

The frequency response of combustor total pressure to spray nozzle pressure perturbations is presented in figure 22. Appropriate values for ignition delay and combustion lag were obtained from the experimental test results of reference 8 for inclusion in the simulation. As a result, the dynamic response of the combustor exit pressure of the simulation was closely matched to the engine experimental data.



(a) Amplitude ratio.



(b) Phase angle.

Figure 21. - Analytical frequency response of combustor total pressure to spray nozzle pressure perturbations.

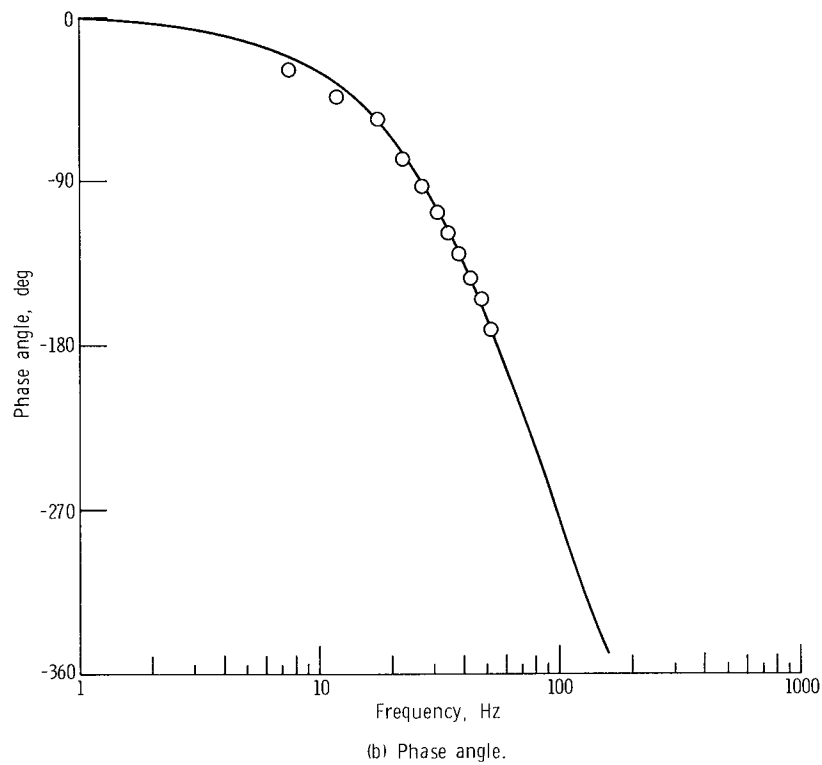
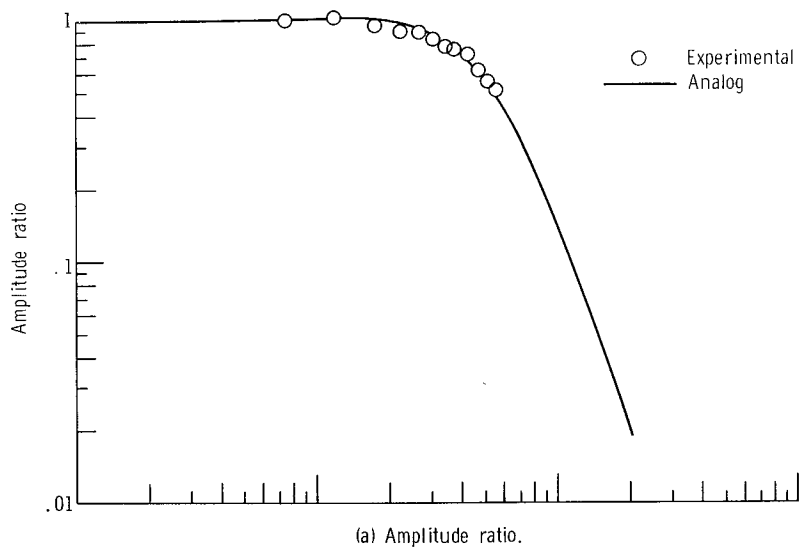
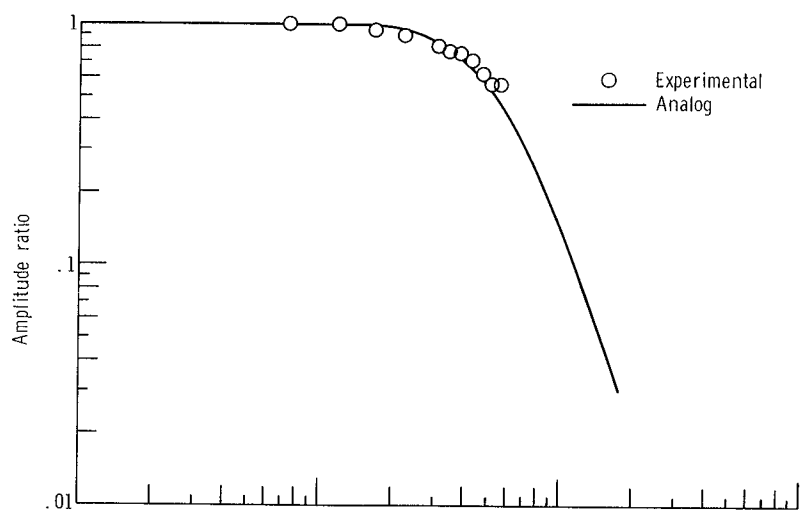
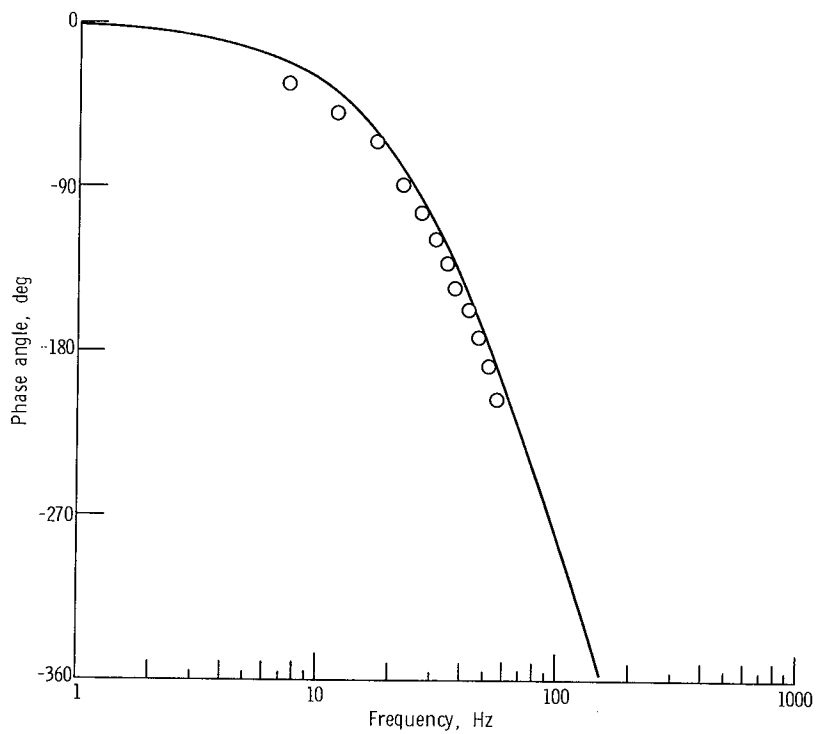


Figure 22. - Frequency response of combustor total pressure to spray nozzle pressure perturbations.

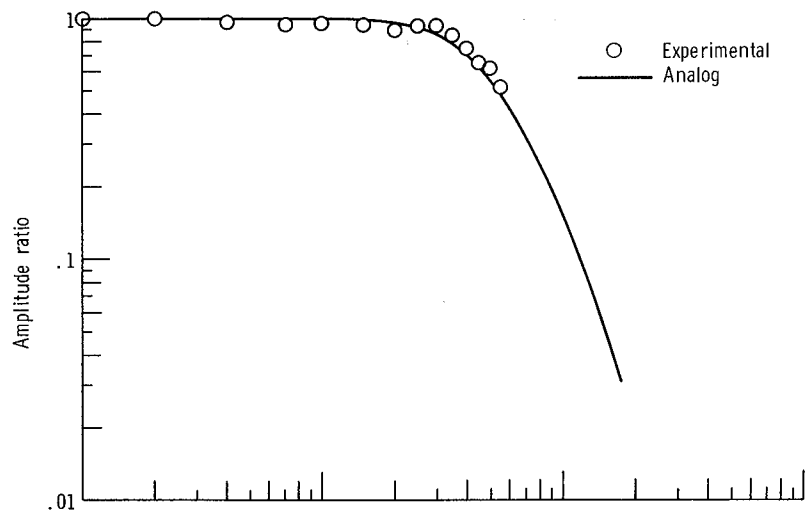


(a) Amplitude ratio.

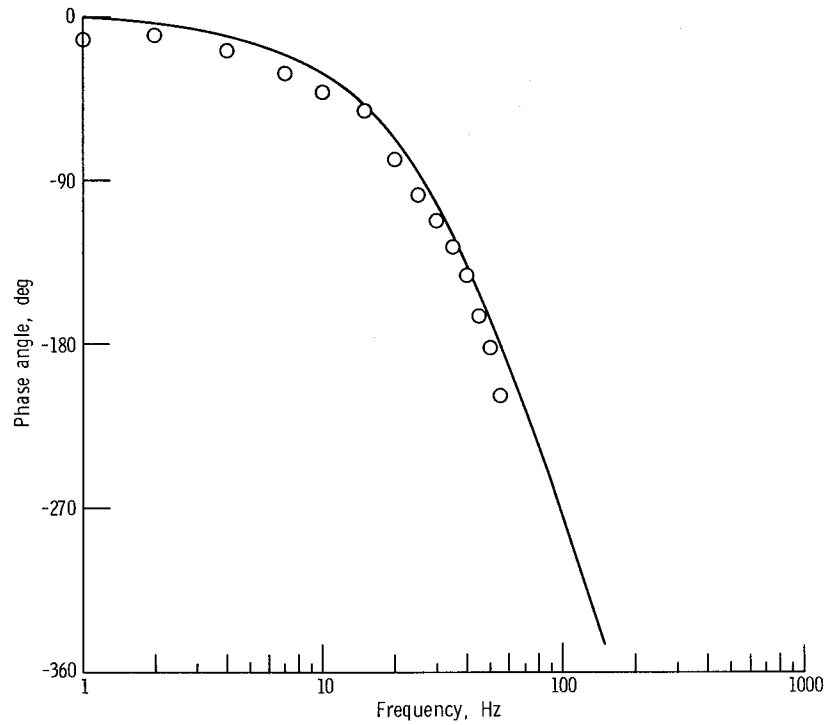


(b) Phase angle.

Figure 23. - Frequency response of compressor discharge total pressure to spray nozzle pressure perturbations.

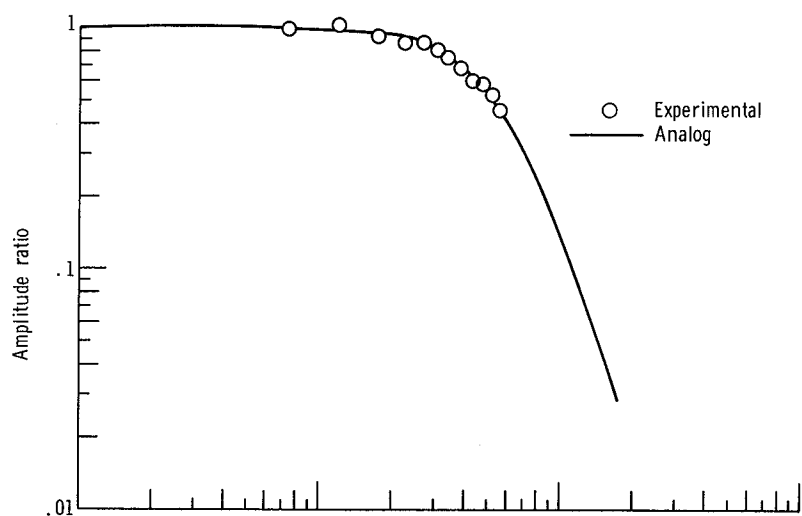


(a) Amplitude ratio.

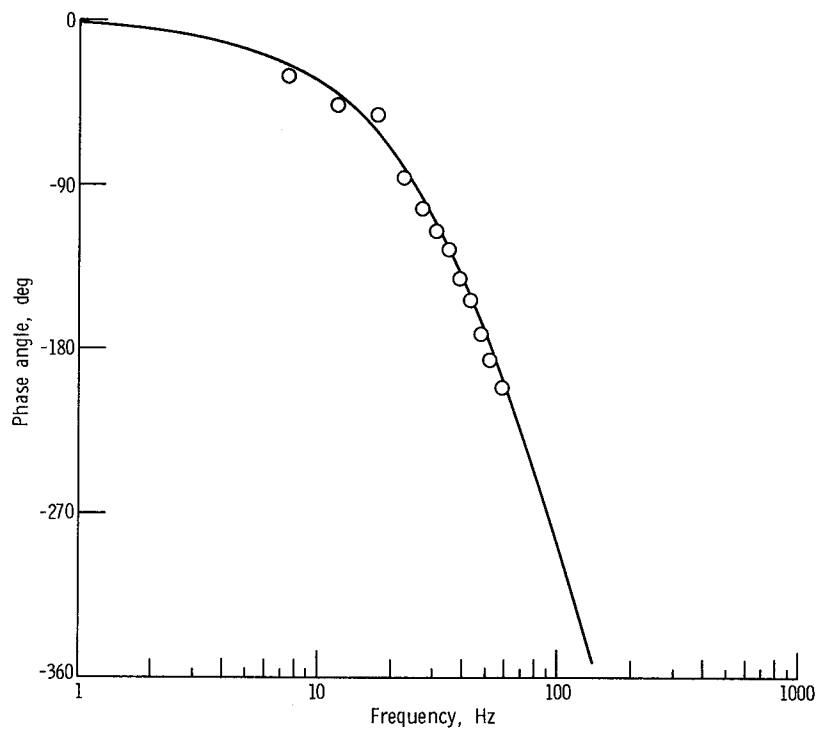


(b) Phase angle.

Figure 24. - Frequency response of compressor discharge static pressure to spray nozzle pressure perturbations.

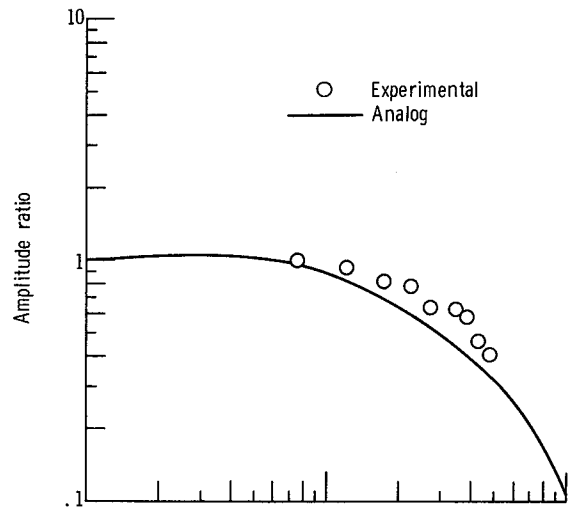


(a) Amplitude ratio.

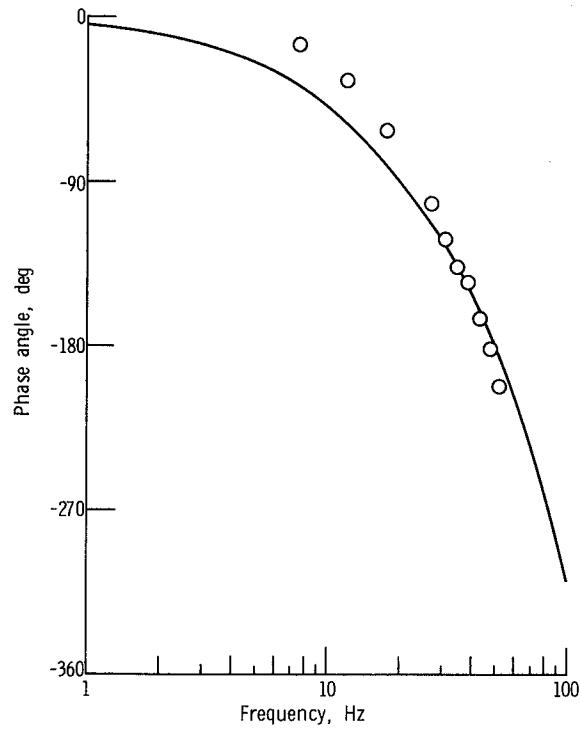


(b) Phase angle.

Figure 25. - Frequency response of compressor sixth-stage discharge static pressure to spray nozzle pressure perturbations.



(a) Amplitude ratio.



(b) Phase angle.

Figure 26. - Frequency response of compressor third-stage discharge static pressure to spray nozzle pressure perturbations.

Compressor

The frequency response of compressor discharge total pressure to spray nozzle pressure is shown in figure 23. The attenuation characteristics are nearly identical; however, a small additional phase shift is exhibited by the actual J85 engine data.

The frequency response of compressor discharge static pressure to spray nozzle pressure is presented in figure 24. The conversion from total to static pressure was accomplished with a linearized conversion formula based on pressure and flow that was obtained from reference 7.

The frequency response of the sixth-stage static pressure to spray nozzle pressure is presented in figure 25. The normalized frequency response curves for the sixth stage are quite similar to the compressor discharge responses when they are perturbed with a fuel flow disturbance due to the small volume between these stages.

The amplitude of upstream compressor stage pressures are less sensitive to fuel flow disturbances than the downstream stage pressures. This trend was exhibited by the third-stage response. The amplitude of the pressure variations become extremely small near the compressor face, thus inaccuracies in the test data can exist. The response of compressor third-stage static pressure to spray nozzle pressure is shown in figure 26. It should be noted that there is some deviation between the analytical and experimental results in the low frequency region.

It should be noted that, in general, the phase shift of the actual J85 engine is slightly higher than that obtained for the engine model. The slight difference can be attributed to the rotor dynamics effect at low frequencies. The analytical phase shift of combustion to spray nozzle pressure (fig. 21(b)) indicates that additional phase shift is obtained from the rotor dynamics. It is probable that if the speed effect had been included during the frequency-response determinations, better agreement between experimental and analytical results could have been obtained at frequencies below 10 hertz.

SUMMARY OF RESULTS

Overall, the results of this study indicate the validity of the simulation over the range investigated, considering, of course, the accuracy of the experimental data to which it was compared. The techniques used in the simulation can be applied to other engines to obtain reasonably accurate steady-state and transient representations.

The study confirms that a mathematical representation using the dynamics inherent in the conservation equations and engine geometry will provide a better simulation than those using component representation and linearized dynamics. The flexibility and wide-

range nonlinear capability outweigh the large equipment complement. The dynamic stage stacking technique reproduces the experimental steady-state compressor operating map very well and provides a method of predicting the stall line as well. This technique is a strong analytical tool especially for engine studies where the stall line is not known.

The technique also provides the capability to couple inlet dynamics to the engine and predict propulsion system interaction.

The combustor representation seems to be the least rigorous in the engine simulation. The difficulty lies in obtaining a simple, but complete, representation of the complicated process.

The results also indicate that care should be exercised in assuming constant speed for simulated dynamic response.

Lewis Research Center,
National Aeronautics and Space Administration,
Cleveland, Ohio, September 24, 1971,
132-15.

APPENDIX A

SYMBOLS

A	area, m^2 ; ft^2	K_D	coefficient, $(kg)(m^2)(K^{1/2})/(N)(sec)$; $(lbm)(ft^2)(^{\circ}R^{1/2})/(lbf)(sec)$
a	speed of sound, m/sec; ft/sec	K_G	coefficient, $(N)(sec)/(kg)(m^2)$; $(lbf)(sec)/(lbm)(ft^2)$
C_n	coefficient, rpm^2/K ; $rpm^2/^{\circ}R$	K_n	coefficient, $(rpm)(sec)/m$; $(rpm)(sec)/ft$
c_p	specific heat at constant pressure, $J/(g)(K)$; $Btu/(lbm)(^{\circ}R)$	K_R	coefficient, $(N)(sec)/(kg)(m^2)$; $(lbf)(sec)/(lbm)(ft^2)$
c_v	specific heat at constant volume, $J/(g)(K)$; $Btu/(lbm)(^{\circ}R)$	K_g	nozzle parameter, $(kg)(m^2)(K^{1/2})/(N)(sec)$; $(lbm)(ft^2)(^{\circ}R^{1/2})/(lbf)(sec)$
g	gravitational constant, $1(kg)(m)/(N)(sec^2)$; 32.17 $(lbm)(ft)/(lbf)(sec^2)$	k_b	bleed flow coefficient, $(kg)(K^{1/2})/(N)(sec)$; $(lbm)(^{\circ}R^{1/2})/(lbf)(sec)$
H	total enthalpy, J/g ; Btu/lbm	L	torque, N-m; ft-lbf
h	static enthalpy, J/g ; Btu/lbm	l	length, m; ft
Δh	actual isentropic expansion value, J/g ; Btu/lbm	M	Mach number
$\Delta h'$	ideal isentropic expansion value, J/g ; Btu/lbm	N	rotational speed, rpm
h_c	heat of combustion, J/g ; Btu/lbm	N'	nonlinear rotational speed, rpm
I	moment of inertia, N-m- sec^2 ; $lbf-ft-sec^2$	n	number of mass particles
J	mechanical equivalent of heat, 1 N-m/J; 778.3 ft-lbf/Btu	P	pressure, N/m^2 ; lbf/ft^2
K	coefficient	\mathcal{P}	power, N-m/sec; ft-lbf/sec
K_A, K_B, K_C	coefficients, $(N^2)(sec^2)/(kg^2)(m^4)(K)$; $(lbf^2)(sec^2)/(lbm^2)(ft^4)(^{\circ}R)$	R	universal gas constant, $287(N)(m)/(kg)(K)$; $53.3 (lbf)(ft)/(lbm)(^{\circ}R)$
		r	mean radius, m; ft
		r_T	tip radius, m; ft
		s	Laplace operator, sec^{-1}
		T	temperature, K; $^{\circ}R$
		$\Delta T'$	ideal total temperature drop across turbine, K; $^{\circ}R$
		t	time, sec

U	mean rotor speed, m/sec; ft/sec	ϕ	flow coefficient
U_T	tip rotor speed, m/sec; ft/sec	ψ^P	pressure coefficient
u	internal energy, J/g; Btu/lbm	ψ^T	temperature coefficient
V	volume, m ³ ; ft ³	ω	angular velocity, sec ⁻¹
v	velocity, m/sec; ft/sec	Subscripts:	
v_θ	tangential velocity, m/sec; ft/sec	b	variable associated with stage bleed
v_z	axial velocity, m/sec; ft/sec	c	variable associated with stage characteristics
v_{zc}	axial velocity associated with stage characteristics, m/sec; ft/sec	f	fuel
W	weight, kg; lbm	G	gas
\dot{W}	weight flow, kg/sec; lbm/sec	(i)	denotes function, i = 1, 2, 3, ...
\dot{W}_f''	externally acted upon fuel flow, kg/sec; lbm/sec	in	inlet
x	distance, m; ft	N	speed
y	distance, m; ft	n	stage number designation
z	distance, m; ft	out	outlet
z'	distance, m; ft	p	variable associated with particle
α	coefficient, 30 sec/min	R	rotor
β	rotor air inlet angle, deg	s	static condition
γ	ratio of specific heats, 1.4	sc	static condition variable associ- ated with stage characteristics
δ	ratio of total pressure to stand- ard atmospheric pressure	stg 1	first stage
η	efficiency	stg 2	second stage
θ	ratio of total temperature to standard atmospheric temper- ature	sv	static condition variable associ- ated with stage volume
λ	work-speed parameter	TC	turbine cooling
ρ	weight density, kg/m ³ ; lbm/ft ³	t	total condition
σ	delay time, sec	tc	total condition variable associated with stage characteristics
τ_A, τ_B	time constant, sec	tr	total condition reference state
		tv	total condition variable associated with stage volume

v variable associated with stage volume
0 free-stream condition
2 compressor inlet
3 compressor discharge

4 combustor
5 turbine
5.1 turbine discharge
8 nozzle

APPENDIX B

BASIC GAS DYNAMICS REPRESENTATION

The relations used for the representation of system gas dynamics can be derived from the continuity, momentum, and energy equations. The mathematical manipulations required to formulate these equations in terms of the chosen variables are given in this appendix.

The laws of conservation of mass, momentum, and energy can be written for quasi-one-dimensional flow as

$$\frac{\partial}{\partial t} (\rho_s A) + \frac{\partial}{\partial x} (\rho_s A v) = 0 \quad (B1)$$

$$\frac{\partial}{\partial t} (\rho_s A v) + \frac{\partial}{\partial x} (\rho_s A v^2) = - A g \frac{\partial P_s}{\partial x} \quad (B2)$$

$$\frac{\partial}{\partial t} (\rho_s A u_t) + \frac{\partial}{\partial x} (\rho_s A v H) = 0 \quad (B3)$$

Continuity equation:

Noting that $\dot{W} = \rho_s A v$, equation (B1) becomes

$$\frac{\partial}{\partial t} (\rho_s A) = - \frac{\partial}{\partial x} \dot{W} \quad (B4)$$

or

$$\frac{\partial}{\partial t} (\rho_s) = - \frac{1}{A} \frac{\partial}{\partial x} \dot{W} \quad (B5)$$

and, lumping in the spatial variable

$$\frac{d}{dt} (\rho_s) = \frac{1}{V} (\dot{W}_1 - \dot{W}_2) \quad (B6)$$

Momentum equation:

Substituting $\dot{W} = \rho_s A v$ into equation (B2) yields

$$\frac{\partial}{\partial t} (\dot{W}) + \frac{\partial}{\partial x} (\rho_s A v^2) = - A g \frac{\partial P_s}{\partial x} \quad (B7)$$

Neglecting the convective momentum term $\partial/\partial x (\rho_s A v^2)$ gives

$$\frac{\partial}{\partial t} (\dot{W}) = - A g \frac{\partial P_s}{\partial x} \quad (B8)$$

or in lumped form

$$\frac{d}{dt} (\dot{W}) = \frac{A g}{l} (P_{s,1} - P_{s,2}) \quad (B9)$$

Energy equation:

Substituting the term $\dot{W} = \rho_s A v$ directly into equation (B3) gives

$$\frac{\partial}{\partial t} (\rho_s A u_t) + \frac{\partial}{\partial x} (\dot{W} H) = 0 \quad (B10)$$

which becomes

$$\frac{\partial}{\partial t} (\rho_s c_v T_t) = - \frac{1}{A} \frac{\partial}{\partial x} (\dot{W} c_p T_t) \quad (B11)$$

or

$$\frac{d}{dt} (\rho_s T_t) = \frac{\gamma}{V} (\dot{W}_1 T_{t,1} - \dot{W}_2 T_{t,2}) \quad (B12)$$

APPENDIX C

STEADY-STATE COMPRESSOR STAGE REPRESENTATION

The mathematical description of the steady-state compressor characteristics is based on the stage-stacking technique. This method uses two-dimensional maps to represent each stage. The individual stage performance is described by a pressure coefficient ψ^P and a temperature coefficient ψ^T as functions of a flow coefficient φ . The coefficients are mathematically described by

$$\psi^P = 2gJ \frac{\Delta h'}{U_T^2} \quad (C1)$$

$$\psi^T = 2gJ \frac{\Delta h}{U_T^2} \quad (C2)$$

$$\varphi = \frac{(v_z/\sqrt{\theta})}{(U/\sqrt{\theta})} \quad (C3)$$

The total enthalpy rise for the n^{th} stage can be related to the stage total pressure ratio from

$$\Delta h'_{tc,n} = c_p T_{tv,n-1} \left[\left(\frac{P_{tc,n}}{P_{tv,n-1}} \right)^{(\gamma-1)/\gamma} - 1 \right] \quad (C4)$$

The adiabatic enthalpy rise can be computed from

$$\Delta h_{tc,n} = c_p (T_{tc,n} - T_{tv,n-1}) \quad (C5)$$

and the stage wheel speed U_T from the relation

$$U_T = \frac{\pi N r_T}{\alpha} \quad (C6)$$

The magnitudes of the inlet pressures and temperatures of the n^{th} stage are determined from the exit conditions of the preceding stage. Therefore, equations (C1) to (C3) can

be combined with equations (C4) to (C6) to develop a set of equations for the n^{th} stage.

$$\psi_n^P = \frac{C_n T_{tv, n-1}}{N^2} \left[\left(\frac{P_{tc, n}}{P_{tv, n-1}} \right)^{2/7} - 1 \right] \quad (C7)$$

$$\psi_n^T = \frac{C_n}{N^2} (T_{tc, n} - T_{tv, n-1}) \quad (C8)$$

$$\varphi_n = \frac{K_n}{N} v_{zc, n} \quad (C9)$$

where

$$C_n = \frac{2gJc_p(\alpha)^2}{\pi^2 r_{T, n}^2} \quad (C10)$$

$$K_n = \frac{\alpha}{\pi r_n} \quad (C11)$$

The axial velocity v_z can be computed from the flow, total pressure, and total temperature at the stage inlet. The flow and axial velocity are related by

$$v_z = \frac{\dot{W}}{\rho_s A} \quad (C12)$$

Eliminating the density from equation (C12) with the state equation,

$$P_s = \rho_s R T_s \quad (C13)$$

results in

$$v_z = \frac{\dot{W} R T_s}{A P_s} \quad (C14)$$

or

$$v_z = \frac{\dot{W}R}{A} \frac{T_t}{P_t} \left(1 + \frac{\gamma - 1}{2} M^2 \right)^{1/(\gamma-1)} \quad (C15)$$

Equation (C15) can be written in terms of corrected parameters as

$$\frac{v_z}{\theta} \rho_{tr} = \frac{\dot{W}\sqrt{\theta}}{A\delta} \left(1 + \frac{\gamma - 1}{2} M^2 \right)^{1/(\gamma-1)} \quad (C16)$$

or

$$\frac{\dot{W}\sqrt{\theta}}{A\delta} = \frac{v_z}{\sqrt{\theta}} \left(1 + \frac{\gamma - 1}{2} M^2 \right)^{-1/(\gamma-1)} \quad (C17)$$

It can be shown from the energy equation that

$$\frac{v^2}{a_t^2} = \frac{2Jc_p}{\gamma R} \left(1 - \frac{T_s}{T_t} \right) \quad (C18)$$

Therefore,

$$\frac{T_s}{T_t} = \left[1 - \frac{\gamma - 1}{2} \left(\frac{v}{a_t} \right)^2 \right] = \left[1 + \frac{\gamma - 1}{2} M^2 \right]^{-1} \quad (C19)$$

Combining equations (C17) and (C19) yields

$$\frac{\dot{W}\sqrt{\theta}}{A\delta} = \frac{v_z}{\sqrt{\theta}} \left[1 - \left(\frac{v}{\sqrt{\theta}} \right)^2 \frac{1}{2gJc_p T_{tr}} \right]^{1/(\gamma-1)} \rho_{tr} \quad (C20)$$

The velocity term appearing inside the brackets of equation (C20) is the magnitude of the velocity vector. If the airflow approaches the rotor inlet at an angle β , then

$$v_z = v \cos \beta \quad (C21)$$

and equation (C20) becomes

$$\frac{\dot{W}\sqrt{\theta}}{\delta A} = \frac{v_z}{\sqrt{\theta}} \left[1 - \left(\frac{v_z}{\sqrt{\theta}} \right)^2 \frac{1}{2gJc_p T_{tr} \cos^2 \beta} \right]^{1/(\gamma-1)} \rho_{tr} \quad (C22)$$

Equation (C22) can be rewritten for the n^{th} stage as

$$\frac{\dot{W}_{c,n}\sqrt{\theta_{v,n-1}}}{A_{c,n}\delta_{v,n-1}} = \frac{v_{zc,n}}{\sqrt{\theta_{v,n-1}}} \left[1 - \left(\frac{v_{zc,n}}{\sqrt{\theta_{v,n-1}}} \right)^2 \frac{1}{2gJc_p T_{tr} \cos^2 \beta_n} \right]^{1/(\gamma-1)} \rho_{tr} \quad (C23)$$

APPENDIX D

STAGE GAS DYNAMICS

The gas dynamics of each compressor stage are assumed to occur in an equivalent stage volume. This stage volume is located downstream of the stage pressure and temperature rise characteristics. The stage gas dynamics are represented by continuity, energy, and momentum balances across the volume.

Assuming that no work is performed in the volume and that the net heat input is negligible, an energy balance can be written for the n^{th} volume as

$$V_n \frac{d}{dt} (\rho_{sv,n} u_{tv,n}) = h_{tc,n} \dot{W}_{c,n} - h_{tv,n} \dot{W}_{c,n+1} \quad (D1)$$

Since $u_t = c_v T_t$ and $h_t = c_p T_t$, equation (D1) becomes

$$\frac{d}{dt} (\rho_{sv,n} T_{tv,n}) = \frac{\gamma}{V_n} (T_{tc,n} \dot{W}_{c,n} - T_{tv,n} \dot{W}_{c,n+1}) \quad (D2)$$

To determine the density of the gas in the stage volume, it is assumed that the rate of change of the static density is proportional to the net weight flow.

$$\frac{d}{dt} (\rho_{sv,n}) = \frac{1}{V_n} (\dot{W}_{c,n} - \dot{W}_{c,n+1}) \quad (D3)$$

The total pressure in the volume can be computed from the equation of state:

$$P_{tv,n} = R \left(1 + 0.2 M_{v,n}^2 \right)^{5/2} \rho_{sv,n} T_{tv,n} \quad (D4)$$

A momentum balance across the stage and associated volumes is used to determine the weight flow into each stage. The flow acceleration is caused by the difference between the static compressor pressure rise $\Delta P_{sc,n}$ and the pressure rise $(P_{sv,n} - P_{sv,n-1})$ imposed by the two stage volumes. This yields

$$\frac{d}{dt} (\dot{W}_{c,n}) = \frac{A_n g}{l_n} [\Delta P_{sc,n} - (P_{sv,n} - P_{sv,n-1})] \quad (D5)$$

However, the inlet conditions to the stage are equal to the outlet conditions of the preceding stage volume, thus $\Delta P_{sc,n} = P_{sc,n} - P_{sv,n-1}$ and equation (D5) reduces to

$$\frac{d}{dt} (\dot{W}_{c,n}) = \frac{A_n g}{l_n} (P_{sc,n} - P_{sv,n}) \quad (D6)$$

If the Mach number at the stage exit and in the volume are identical, then equation (D6) can be written in the form

$$\frac{d}{dt} (\dot{W}_{c,n}) = \frac{A_n g}{l_n} (P_{tc,n} - P_{tv,n}) (1 + 0.2M^2)^{-7/2} \quad (D7)$$

Equations (D2) to (D4) and (D7) are used to represent the gas dynamics of the n^{th} volume. The simulation neglects the difference between static and total pressures due to the difficulty in computing the Mach number. Neglecting this effect results in a slight error in equations (D4) and (D7). Since the interstage Mach numbers within the compressor are less than 0.5, the range of corrections for equations (D4) and (D7) are

$$1.0 < (1 + 0.2M^2)^{5/2} < 1.13$$

$$0.84 < (1 + 0.2M^2)^{-7/2} < 1.0$$

The maximum error introduced by this simplification is about 15 percent; however, this approximation is only reflected in the dynamic performance and does not alter the steady-state characteristics. This fact can be readily observed from the computation technique shown by the block diagram (fig. 27). The conversion from static to total values is essentially accomplished through coefficient potentiometers 1 to 3, which are inputs to the integrators. Coefficient potentiometer 6 is used to convert total to static density and thus merely removes the correction introduced by potentiometer 1. Since both integrator input potentiometers are identical, only the dynamic performance of the compressor will be altered.

In the steady-state case, the expressions (D2), (D3), and (D7) become

$$\frac{\gamma}{V_n} (T_{tc,n} \dot{W}_{c,n} - T_{tv,n} \dot{W}_{c,n+1}) = 0 \quad (D8)$$

$$\frac{1}{V_n} (\dot{W}_{c,n} - \dot{W}_{c,n+1}) = 0 \quad (D9)$$

$$\frac{A_{ng}}{l_n} (P_{tc,n} - P_{tv,n}) = 0 \quad (D10)$$

which implies that

$$\dot{W}_{c,n} = \dot{W}_{c,n+1} \quad (D11)$$

$$P_{tc,n} = P_{tv,n} \quad (D12)$$

$$T_{tc,n} = T_{tv,n} \quad (D13)$$

From equations (D11) to (D13), it is evident that the steady-state results are not affected by the approximations in the volume dynamics.

Interstage bleed can be included in the compressor simulation by modifying equations (D2) and (D3). The bleed flow can be computed from the relation

$$\dot{W}_{b,n} = k_b A_{b,n} \frac{P_{tv,n}}{\sqrt{T_{tv,n}}} \quad (D14)$$

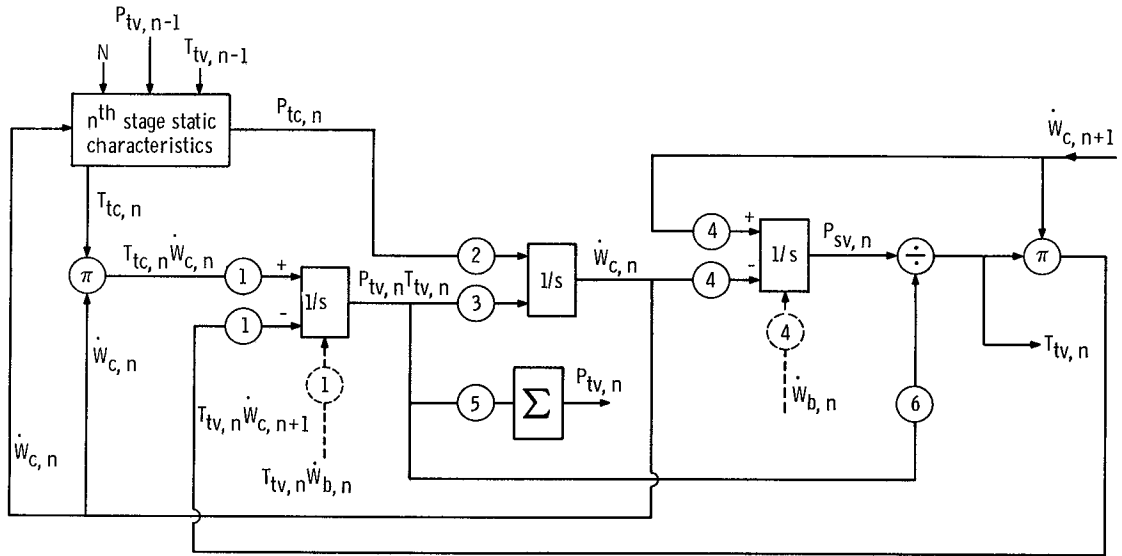
Including the effects of interstage bleed allows equations (D2) and (D3) to become

$$\frac{d}{dt} (\rho_{sv,n} T_{tv,n}) = \frac{\gamma}{V_n} (T_{tc,n} \dot{W}_{c,n} - T_{tv,n} \dot{W}_{c,n+1} - T_{tv,n} \dot{W}_{b,n}) \quad (D15)$$

$$\frac{d}{dt} (\rho_{sv,n}) = \frac{1}{V_n} (\dot{W}_{c,n} - \dot{W}_{c,n+1} - \dot{W}_{b,n}) \quad (D16)$$

The inclusion of bleed flow is shown dashed in figure 27. The steady-state flow through the compressor is altered by the interstage bleed by forcing the flow of the $(n+1)^{th}$ stage to a lower value.

As noted in figure 27, the simplification introduced by neglecting the effects of static to total conversion only affects the dynamic performance of the compressor.



Coefficients

- | | |
|-----------------------------------------------|---------------------------|
| 1. $\frac{\gamma}{V_n} (1 + 0.2 M^2)^{5/2}$ | 4. $1/V_n$ |
| 2. $\frac{A_n g}{l_n} (1 + 0.2 M^2)^{-7/2}$ | 5. R |
| 3. $\frac{A_n g}{l_n} R (1 + 0.2 M^2)^{-7/2}$ | 6. $(1 + 0.2 M^2)^{-5/2}$ |

Figure 27. - Block diagram for n^{th} stage computation.

APPENDIX E

BIVARIANT FUNCTION GENERATION

The need arises in the compressor and turbine simulations to generate functions of two variables. In general, bivariate function generation is difficult with pure analog devices. A number of schemes varying primarily in complexity are available for analog use.

The functions here required are nonlinear empirical functions of two variables, which are not separable into functions of single variables. We, therefore, required a three-dimensional surface. If the functions were separable, they could be separated into two single-variable functions and combined in some algebraic manner.

Among the techniques available are correlation, curve fitting, and multicurve interpolation.

Correlation. - There is a possibility that a single-parameter correlation between the variables does exist. An analysis based on this premise is developed and applied to the turbine data in appendix F.

Curve fitting. - Another analytical technique frequently used is curve fitting. The family of curves of one variable are individually fitted, and the coefficients plotted on diode function generators. These are then used in a circuit that generates the type of curve required; for example, power, exponential, and so forth. Accuracy and frequency response are very good if all electronic components can be used and interpolation between curves is minimized. However, a large complement of equipment is required.

A typical coefficient plot and block diagram for a third-order power curve fit of the turbine enthalpy function is shown in figures 28 and 29, respectively. The curves are

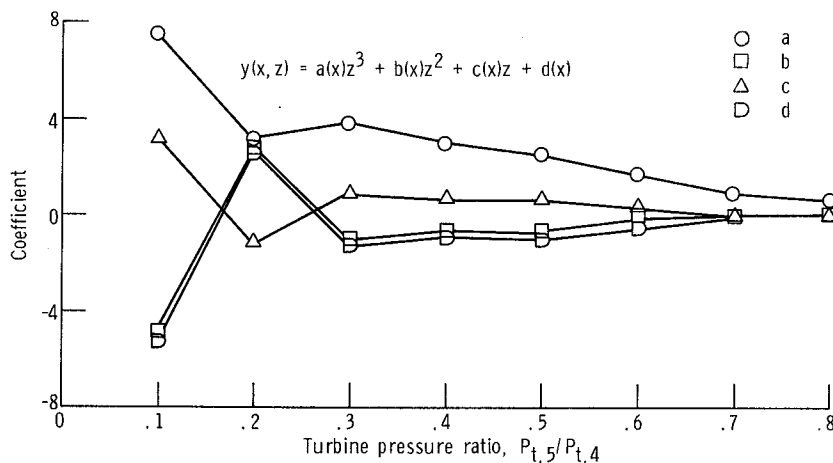


Figure 28. - Typical coefficient variation for third-order bivariate function generator.

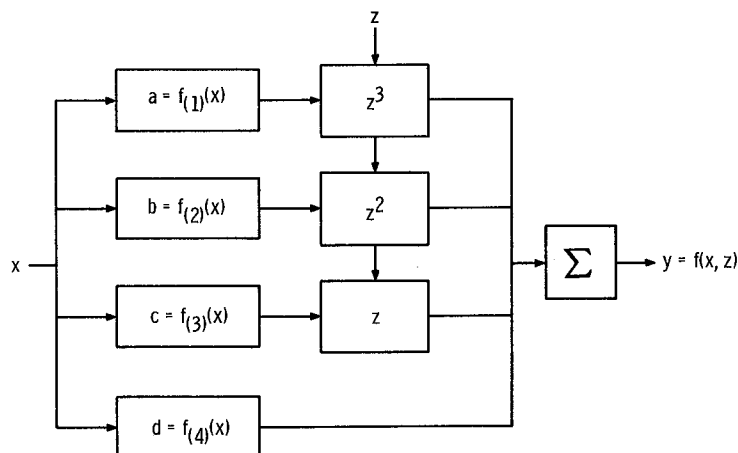


Figure 29. - Block diagram of bivariate function generation using typical third-order curve fit.

reasonably well behaved and lend themselves to easy simulation. Errors can occur through assuming linear interpolation between points. This could be improved by taking nonuniform input segments.

Multicurve interpolation. - Diode function generators and tapped potentiometer servo groups can also be used to produce functions of two variables. Various interpolation schemes have been developed to increase response and reduce the amount of equipment. This method is particularly amenable to the turbine simulation because of the low-frequency nature of speed and the high-frequency nature of pressure ratio.

Diode function generators are used to generate various members of the family of curves for constant values of the low-frequency variable. The high-frequency variable is their input. The simultaneous outputs of these generators are applied to the taps of a servo potentiometer, which is driven by the low-frequency variable. The servo multipliers can be replaced by electronic multipliers.

For the J85 turbine, the corrected speed is the low-frequency variable. The three curves for constant corrected speed were chosen to represent the enthalpy and flow performance over a range of turbine pressure ratios, the high-frequency variable. Outputs were applied to the end and center taps of the servo potentiometer, which was driven by the corrected speed parameter.

The voltage on the taps varied inversely with the corrected speed and the servo interpolates linearly between the curves. To compensate for this, the corrected speed signal was modified by another function generator that alters the servo input resulting in a nonlinear interpolation.

A typical block diagram for this scheme is shown in figure 30. The nonlinear correction is given in figure 31.

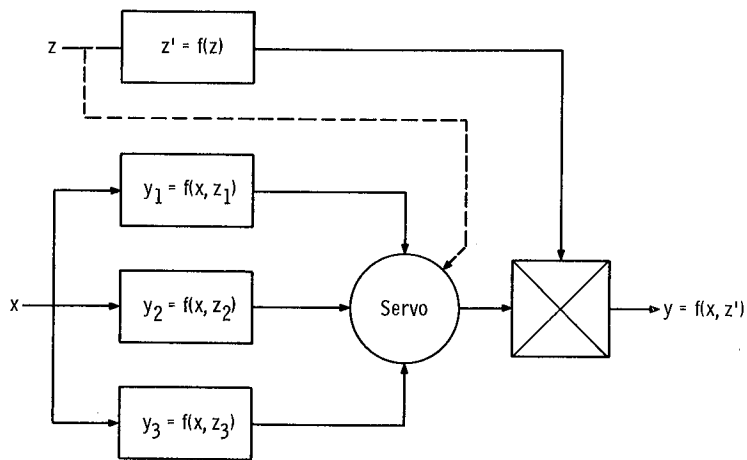


Figure 30. - Typical block diagram for an optimized bivariate function generator.

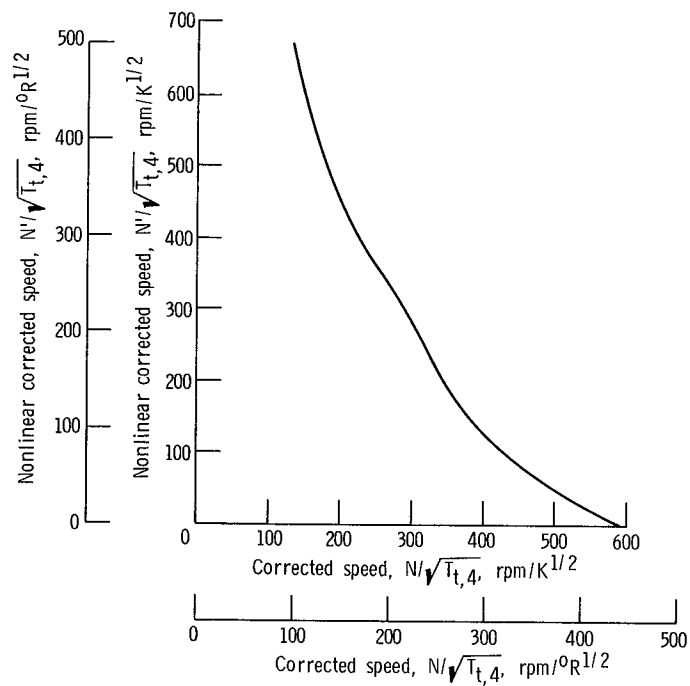


Figure 31. - Nonlinear correction of corrected speed for bivariate function generation.

APPENDIX F

TURBINE PERFORMANCE CORRELATION

A method is developed in this appendix by which the performance of a turbine can be analytically represented for simulation over a range of operating variables. The method uses the equivalence of momentum and energy as a basis. With an analytical expression for efficiency, the correlation is performed in terms of engineering variables and parameters.

The fundamental relation of torque and rate of change of angular momentum, as applied to a rotating mass particle, is derived from Newton's second law:

$$L_p = \frac{d}{dt} \frac{r}{g} W v_\theta \quad (F1)$$

Assuming a fixed, or average, radius of rotation and expanding the differential result in

$$L_p = \frac{r}{g} \left(W \frac{dv_\theta}{dt} + v_\theta \frac{dW}{dt} \right) \quad (F2)$$

In difference form this becomes

$$L_p = \frac{r}{g} \left(W \frac{\Delta v_\theta}{\Delta t} + v_\theta \frac{\Delta W}{\Delta t} \right) \quad (F3)$$

Each particle of mass passing through a point will experience this same change in momentum in Δt time. If n particles flow in time Δt , the resultant torque is the summation of the momentum change for each particle, or

$$L = \frac{r}{g} \left(nW \frac{\Delta v_\theta}{\Delta t} + v_\theta \frac{\Delta nW}{\Delta t} \right) \quad (F4)$$

But, weight flow rate is defined as

$$\dot{W} = \frac{nW}{\Delta t} \quad (F5)$$

so that

$$L = \frac{r}{g} (\dot{W} \Delta v_{\theta} + v_{\theta} \Delta \dot{W}) \quad (F6)$$

For steady flow conditions

$$L = \frac{r}{g} \dot{W} \Delta v_{\theta} \quad (F7)$$

For a rotary machine, the power is given by

$$\mathcal{P} = LW \quad (F8)$$

and

$$U = rW \quad (F9)$$

Combining equations (F7) to (F9) gives

$$\mathcal{P} = \frac{U}{g} \dot{W} \Delta v_{\theta} \quad (F10)$$

which is the power output in terms of angular momentum.

Consider now the performance of a turbine from the energy viewpoint. The general energy equation derived from the first law of thermodynamics gives

$$\mathcal{P} = \eta J \frac{d}{dt} W c_p T_t \quad (F11)$$

for a quasi-steady process, where the efficiency η refers to turbine overall efficiency. Assuming a constant specific heat gives

$$\mathcal{P} = \eta J \left(W c_p \frac{dT_t}{dt} + c_p T_t \frac{dW}{dt} \right) \quad (F12)$$

Or, as before, in difference form

$$\mathcal{P} \approx \eta J \left(\dot{W} c_p \Delta T_t' + c_p T_t \frac{\Delta W}{\Delta t} \right) \quad (F13)$$

where $\Delta T'_t$ refers to the ideal total temperature drop across the turbine. This reduces for steady state to

$$\mathcal{P} = \eta J \dot{W} c_p \Delta T'_t \quad (\text{F14})$$

which represents the power output in terms of energy.

Proceeding with the isentropic relations between pressure and temperature, equation (F14), in terms of pressure ratio, becomes

$$\mathcal{P} = \eta J \dot{W} c_p T_{t, \text{in}} \left[1 - \left(\frac{P_{t, \text{out}}}{P_{t, \text{in}}} \right)^{(\gamma-1)/\gamma} \right] \quad (\text{F15})$$

Defining

$$v_s = \sqrt{g J c_p T_{t, \text{in}} \left[1 - \left(\frac{P_{t, \text{out}}}{P_{t, \text{in}}} \right)^{(\gamma-1)/\gamma} \right]} \quad (\text{F16})$$

as the spouting velocity, equation (F15) becomes

$$\mathcal{P} = \eta \frac{\dot{W}}{g} v_s^2 \quad (\text{F17})$$

Eliminating power between the momentum and energy relations, equations (F10) and (F17), respectively, yields

$$U \Delta v_\theta = \eta v_s^2 \quad (\text{F18})$$

or, solving for efficiency

$$\eta = \frac{U}{v_s} \cdot \frac{\Delta v_\theta}{v_s} \quad (\text{F19})$$

Stewart, in reference 9, gives an assumed general relation of efficiency as a function of an overall work-speed parameter:

$$\eta = f(\lambda) \quad (\text{F20})$$

where

$$\lambda = \frac{U^2}{gJ \Delta h} = \frac{U^2}{v_s^2} = \left(\frac{U}{v_s} \right)^2 \quad (\text{F21})$$

Hence,

$$\eta = f_{(1)} \left(\frac{U}{v_s} \right) \quad (\text{F22})$$

Since $\Delta v_\theta / v_s$ is not a constant, equations (F19) and (F22) imply that

$$\frac{\Delta v_\theta}{v_s} = f_{(2)} \left(\frac{U}{v_s} \right) \quad (\text{F23})$$

In terms of measurable variables

$$\frac{\Delta h}{U v_s} = f_{(3)} \left(\frac{U}{v_s} \right) \quad (\text{F24})$$

or

$$\frac{\Delta h}{N \sqrt{T_{t, \text{in}}} f \left(\frac{P_{t, \text{out}}}{P_{t, \text{in}}} \right)} = f \left[\frac{N}{\sqrt{T_{t, \text{in}}} f \left(\frac{P_{t, \text{out}}}{P_{t, \text{in}}} \right)} \right] \quad (\text{F25})$$

where

$$f \left(\frac{P_{t, \text{out}}}{P_{t, \text{in}}} \right) = \sqrt{1 - \left(\frac{P_{t, \text{out}}}{P_{t, \text{in}}} \right)^{(\gamma-1)/\gamma}} \quad (\text{F26})$$

This is the general functional relation for the theoretical performance of a turbine based on the efficiency relation of Stewart.

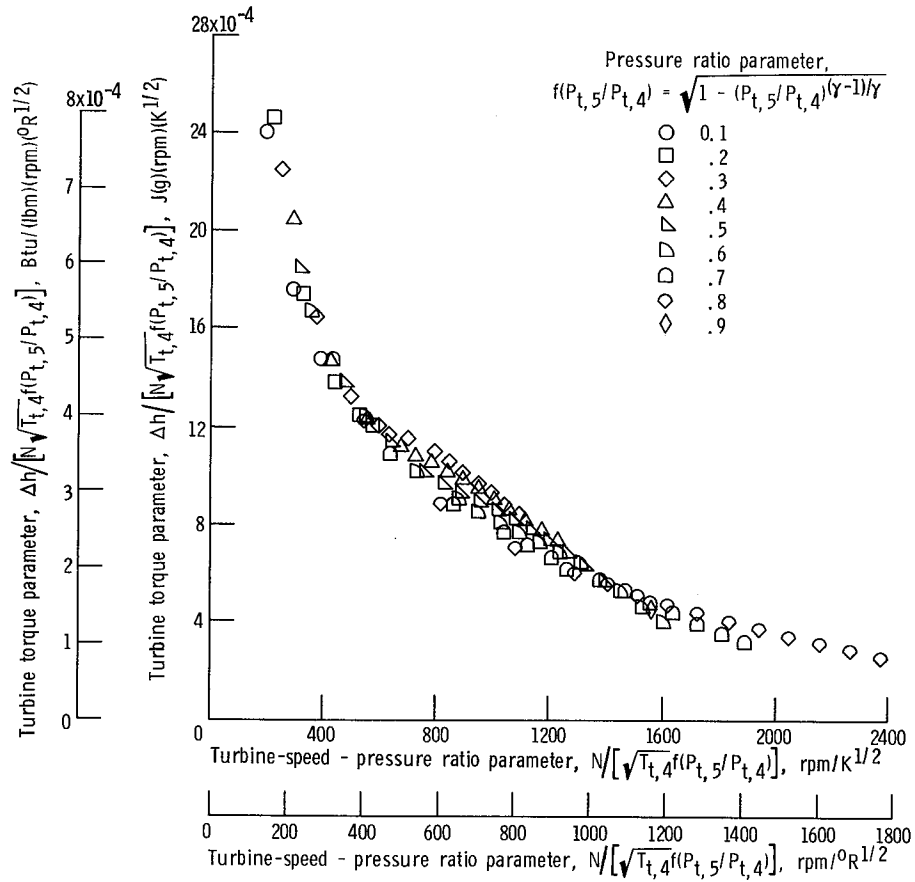


Figure 32. - Turbine torque performance correlation.

The relation shows that the turbine performance can be expressed as a function of a single parameter. This makes it most amenable to simulation.

The correlation was applied to the turbine overall performance shown in figure 11. The results are plotted in figure 32. The correlation is generally good. The midrange shows effects of a variable perhaps not included in the analysis. Some scatter can also be attributed to interpolation of the basic turbine data.

Examination of the turbine flow performance shown in figure 14 suggests that the well known nozzle flow parameter

$$\frac{\dot{W} \sqrt{T_t}}{P_t} = K_D f \left(\frac{P_s}{P_t} \right) \quad (F27)$$

could be used to correlate the data as a function of a single variable.

Since a turbine consists of alternating stator blades or nozzles and rotating blades, expansion occurs in the stators and may also occur in the rotors. Thus, the flow

through a turbine stage can be represented by

$$\frac{\dot{W} \sqrt{T_t}}{P_t} = K_D \left(\frac{P_s}{P_t} \right)^{1/\gamma} \sqrt{1 - \left(\frac{P_s}{P_t} \right)^{(\gamma-1)/\gamma}} \quad (\text{F28})$$

where P_s/P_t is the stage pressure ratio.

If the stage pressure ratio is assumed to be equal for all stages of a multistage turbine, then

$$\left(\frac{P_s}{P_t} \right)_5 = \left(\frac{P_s}{P_t} \right)_{\text{stg 1}} \left(\frac{P_s}{P_t} \right)_{\text{stg 2}} \dots \left(\frac{P_s}{P_t} \right)_n \quad (\text{F29})$$

or

$$\left(\frac{P_s}{P_t} \right)_5 = \left(\frac{P_s}{P_t} \right)_n^n \quad (\text{F30})$$

Thus for the overall turbine flow

$$\left(\frac{\dot{W} \sqrt{T_t}}{P_t} \right)_5 = K_D \left(\frac{P_s}{P_t} \right)_5^{1/n\gamma} \sqrt{1 - \left(\frac{P_s}{P_t} \right)_5^{(\gamma-1)/n\gamma}} \quad (\text{F31})$$

or

$$\frac{\dot{W} \sqrt{T_t}}{P_t f \left(\frac{P_s}{P_t} \right)} = K_D \quad (\text{F32})$$

However, it has been shown experimentally that this flow correlation varies as a function of the speed parameter $N/\sqrt{T_t}$. We have, finally, a correlation of the form

$$\frac{\dot{W} \sqrt{T_t}}{P_t f \left(\frac{P_s}{P_t} \right)} = f \left(\frac{N}{\sqrt{T_t}} \right) \quad (\text{F33})$$

The results of this correlation, as applied to the J85 turbine performance data with $n = 2$, are shown in figure 33.

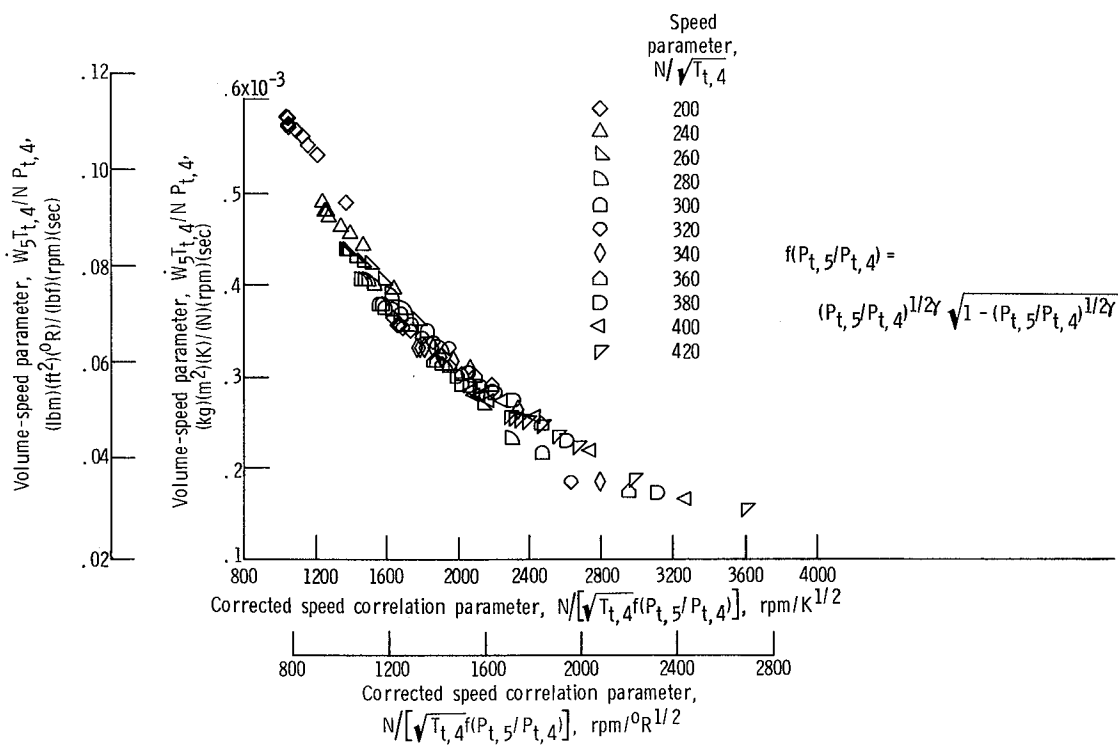


Figure 33. - Turbine flow correlation.

REFERENCES

1. Kuhlberg, J. F.; Sheppard, D. E.; King, E. O.; and Baker, J. R.: The Dynamic Simulation of Turbine Engine Compressors. Paper 69-486, AIAA, June 1969.
2. Willoh, Ross G.; and Seldner, Kurt: Multistage Compressor Simulation Applied to the Prediction of Axial Flow Instabilities. NASA TM X-1880, 1969.
3. Turner, L. Richard; and Lord, Albert M.: Thermodynamic Charts for the Computation of Combustion and Mixture Temperatures at Constant Pressure. NACA TN 1086, 1946.
4. Calogeras, James E.: Experimental Investigation of Dynamic Distortion in a Mach 2.50 Inlet with 60 Percent Internal Contraction and Its Effect on Turbojet Stall Margin. NASA TM X-1842, 1969.
5. Wasserbauer, Joseph F.: Dynamic Response of a Mach 2.5 Axisymmetric Inlet with Engine or Cold Pipe and Utilizing 60 Percent Supersonic Internal Area Contraction. NASA TN D-5338, 1969.
6. Johnsen, Irving A.; and Bullock, Robert O.: Aerodynamic Design of Axial-Flow Compressors. NASA SP-36, 1965.
7. Willoh, Ross G.: A Mathematical Analysis of Supersonic Inlet Dynamics. NASA TN D-4969, 1968.
8. Szuch, John R.; Paulovich, Francis J.; and Bruton, William M.: A Study of Turbojet Combustor Dynamics Using Sweep Frequency Data. NASA TN D-6084, 1970.
9. Stewart, Warner L.: Analytical Investigation of Multistage-Turbine Efficiency Characteristics in Terms of Work and Speed Requirements. NACA RM E57K22b, 1958.

